Unraveling the inhibitory mechanism of adenylyl cyclase 8E: New insights into regulatory pathways of cAMP signal integration

Yohan Legueux-Cajgfinger, Mahesh Velusamy, Samar Fathallah, Benjamin Vallin, Laurent Duca, Manuel Dauchez, Pierre Vincent, Isabelle Limon, Régis Blaise

Unraveling the inhibitory mechanism of adenylyl cyclase 8E: New insights into regulatory pathways of cAMP signal integration.

Authors: Yohan Legueux-Cajgfinger[1,#], Mahesh Velusamy[2,#], Samar Fathallah[1,#], Benjamin Vallin[1], Laurent Duca[2], Manuel Dauchez[2], Pierre Vincent[1, 3], Isabelle Limon[1,§] and Régis Blaise[1,§,*].

Affiliations:

[1] Sorbonne Université, Institut de Biologie Paris-Seine (IBPS), CNRS UMR 8256, Biological Adaptation and Ageing, 7 quai St-Bernard, F-75005, Paris, France.

[2] CNRS UMR 7369, Matrice Extracellulaire et Dynamique Cellulaire (MEDyC), Université de Reims Champagne Ardenne, F-51095 Reims, France.

[3] IGF, Univ. Montpellier, CNRS, INSERM, Montpellier, France

# These authors have contributed equally to this work and share first authorship.

§ These authors have contributed equally to this work and share last authorship.

* Corresponding author Régis Blaise, regis.blaise@sorbonne-universite.fr ;

ABSTRACT

Adenylyl Cyclase 8E (AC8E), which lacks part of M1 transmembrane domain, has been previously shown to dimerize with AC3 and down-regulate its activity, but the molecular mechanism of this inhibitory effect has remained elusive. Here, we first show that AC8E also inhibits AC2 and AC6, highlighting the functional importance of this novel regulatory mechanism in the cAMP signaling pathway across AC families. We then completed the partial structure of Bos taurus AC9 using combinations of comparative modeling and fold recognition methods, and used this as a template to build the first full 3D-models of AC8 and AC8E. These models evidenced that the lack of M1 transmembrane domain of AC8E shifts the N-terminal domain, which impacts the orientation of the helical domains, thus affecting the catalytic site. This was confirmed in living cells with cAMP imaging, where we showed that the N-terminal domain is required for reducing cAMP production. Our data also show that AC8E prevents the translocation of other ACs towards the plasma membrane, further reducing the cAMP responsiveness to extracellular signals. This newly discovered dual inhibitory mechanism provides an additional level of regulation of cAMP-dependent signals integration.

1. INTRODUCTION

The response of cells to their environment strongly depends on the expression and membrane localization of adenylyl cyclases (ACs), which, together with cyclic nucleotide phosphodiesterases (PDEs) and multidrug resistance-associated proteins (MRPs), are the principal enzymes controlling the cAMP signal. Nine membrane forms of AC have been identified in mammals (AC1-9), with discrete tissue distributions and unique regulatory properties, providing a potential focal point within the cell for the integration of diverse stimuli [1,2]. ACs 1 to 9 all have an intracellular N-terminus, two cassettes organized into six membrane spanning domains (M1 and M2) and two cytosolic domains (C1 and C2), each divided into 2 distinct functional a and b units. The regulatory N-terminal, the C1b and the C2b domains have little homologies and determine their unique properties. The C1a and C2a domains, which are the most homologous among AC isoforms, interact together to form the catalytic core responsible for cAMP production [3]; its molecular structure has been modeled associated to G-alphas protein in the late 1990's [1,4–6]. The two transmembrane cassettes are involved in the assembly of ACs allowing for the formation of homo- or hetero-dimers that have often been considered as the functional unit of these enzymes [7,8].

We have recently identified a new family of four short AC8 proteins derived from AC8 RNA splice-variants in inflamed rat vascular smooth muscle cells [9]. They are referred to as AC8E-H, in accordance with the nomenclature of previously identified variants [10–12]. Compared to the full-length AC8 (AC8A), AC8E-H mRNA share an in-frame deletion of 414bp at the end of exon 1, which translates into AC8 proteins lacking the amino acids 180 to 317 forming the first five transmembrane domains (TM1-5) and their linked intracellular and extracellular loops. AC8F, AC8G and AC8H

display the additional deletion of exon 8, exon 11 or both, respectively identified in AC8C, AC8B and AC8D splice variants [9,10,12] encoding for the end of C1b domain and the extracellular loop between TM7 and TM8. Whereas AC8G-H are unstable and poorly expressed, AC8E-F act as dominant-negatives by dimerizing with the full-length AC3, retaining the complex in the endoplasmic reticulum, thereby efficiently inhibiting global cAMP production within the cell [9].

In 2019, a cryo-electron microscopy structure of bovine AC9 lacking the N-terminus and C1b domains was described [13]. Here, we proposed a predicted complete structure of the bovine AC9 using the combination of comparative modeling and fold recognition. We then constructed the complete 3D-models of full-length AC8 (AC8A) and AC8E, using the full AC9 model as a template, leading to highlighting structural changes within AC8E. Based on these structural changes, we set up biochemical and real-time biosensor experiments to unravel the AC8E inhibitory mechanism on cell cAMP production. Our results, combined with our previous study [9], demonstrate that the AC8E-dependent mechanism preventing the signals integration involves the N-terminus and the heterodimerization domain(s).

2. MATERIALS AND METHODS

2.1 Reagents

Dulbecco's modified Eagle's medium (DMEM), type I collagen from calf skin, poly-L-lysine, L-glutamine, penicillin, streptomycin, and 3-isobutyl-1-methylxanthine (IBMX) were purchased from Sigma-Aldrich, Saint-Quentin-Fallavier, France. We obtained fetal calf serum (FCS) and collagenase from Gibco BRL, Cergy-Pontoise, France. Forskolin (fsk) and isoproterenol were obtained from Tocris Bioscience, Bristol, UK. Opti-MEM and NuPAGE LDS sample buffer were obtained from Invitrogen, Life Technologies, Saint-Aubin, France. We purchased the QIAquick Gel Extraction Kit and QIAprep Spin Miniprep Kit from Qiagen, Les Ulis, France. FuGENE HD was purchased from Promega, Charbonnières-les-Bains, France. Halt protease inhibitor cocktail and Pierce™ Anti-HA Magnetic Beads were obtained from Thermo Fisher Scientific, Villebon-sur-Yvette, France. We purchased GelRed from Biotium, Fremont, CA, USA and oligonucleotides from Eurofins Genomics, Les Ulis, France. The DC protein assay and the Clarity western ECL substrate were purchased from Bio-Rad, Marnes-la-Coquette, France. Protein G PLUS-Agarose and G418 were obtained from Santa Cruz Biotechnology, Inc., Dallas, TX, USA. Nitrocellulose membranes were purchased from Amersham, Courtaboeuf, France. Primary antibodies were purchased from Abcam (Paris, France) or Santa Cruz (Santa Cruz Biotechnology, Inc. Heidelberg, Germany); HRP-conjugated secondary antibodies were purchased from Abliance, Compiègne, France. We obtained the cAMP - Gs HiRange kit from Cisbio Bioassays, Codolet, France. Restriction enzymes were obtained from New England Biolabs, Évry, France. Infusion cloning kit and CloneAmp HiFi PCR Premix were purchased from Takara Europe, Saint-Germain-

En-Laye, France. The Dako fluorescence mounting medium from Dako, Carpinteria, CA, USA.

2.2 Molecular modeling and docking

The sequences of adenylate cyclases type 8A (NP_058838.1) and 8E (AWX41284.1) from *Rattus Norvegicus* were retrieved from the NCBI reference sequence database. The best template was selected using protein BLAST against the PDB database. The domains of the above targets were further classified against the identified template AC9 from *Bos taurus* (PDB 6R4O_A and 6R3Q_A with a 4.2Å and 3.4Å resolution, respectively) using a T-coffee server. Subsequently, the helical orientations of transmembrane cassettes M1(TM1-6) and M2 (TM7-12) were defined using various online membrane prediction servers such as TOPCONS, CCTOP, TMHMM, UniProt, MESAT-SVM, Protter and T-Coffee.

The missing domains (N, C1B, and C2B) and loop regions of AC9 were modeled individually using the combinations of comparative modeling and fold recognition [14]. It was carried out using the SWISS-MODEL and Phyre2 servers, respectively. The loops and the helical orientations of the AC8A and AC8E models were defined based on the multiple sequence alignments and cross-validated using diverse servers for membrane prediction. Then, the known and unknown domain models were assembled using protein-protein docking procedure and AIDA *ab-initio* domain assembly server. For this purpose, both blind and site-specific docking was performed on the AC9 and AC8 models against the C1B domain model using both ClusPro and HADDOCK servers, respectively. The models were further refined using the 3D-protein structure refinement server 3Drefine. The detailed analysis of interactions and the molecular surface areas were calculated for the truncated AC8E model to predict its consequence using PyMOL and CASTp servers, respectively .

2.3 Cell culture

HEK-293 cells were grown at 37 °C, under an atmosphere containing 5% CO_2, in DMEM containing 4.5 g·L−1 glucose, 4mM L-glutamine, 5% FCS, 100 U·mL−1 penicillin and 100 µg·mL−1 streptomycin.

2.4 Cloning strategies

Primers used are all given in the **Supplementary Table 1**. The plasmids encoding AC8E, AC3-HA, pcDNA3-HA and $^{T}Epac^{VV}$ are described in Vallin et al., 2018 [9]. The dog AC6 and rat AC2 cDNAs were amplified by PCR and cloned into pcDNA3-HA at the EcoRI-BamHI sites to generate the HA-tagged AC6 or AC2 expression plasmids. AC8EΔNt encoding plasmid was generated from AC8E-encoding plasmid (template plasmid) by a PCR-based strategy deleting the AC8E cDNA base pairs from 4 to 537. The PCR product was recircularized using the infusion cloning kit after removing the template plasmid (DpnI digestion).

pCMV-mEGFP-N1 plasmid was generated by PCR to create the A206K mutation into the EGFP encoding sequence of the pCMV-EGFP-N1 plasmid. The mEGFP-tagged AC8A or AC8E-encoding plasmid was generated by PCR-cloning of AC8A, or AC8E (Supplementary Table 1) in frame with mEGFP into pCMV-mEGFP-N1 plasmid using Infusion cloning kit. All constructs were sequenced on both strands (Eurofins Genomics, les Ulis, France).

2.5 Transitory and stable transfections

Transient and stable transfection of plasmids in HEK293 cells were performed according to the FuGENE HD protocol database as previously described in [9].

For stable transfection, HEK-293 cultured in 100mm dishes were transfected by 10µg of empty pcDNA3 (control), pCDNA3-AC8E or pcDNA3-AC8EΔNt according to the FuGENE HD protocol. After 48h, transfected HEK-293 were treated with 0.8µg·mL−1

of G418 for one week to obtain polyclonal cell populations. Monoclonal cell populations were then generated by limiting dilution and screened by immunoblotting.

2.6 Co-immunoprecipitation and immunoblots

Transiently transfected HEK-293 cells were washed with ice-cold PBS and lysed in 1 mL of RIPA buffer (50 mM Tris pH 7.4, 0.5 mM EDTA, 150 mM NaCl, 0.3% (v/v) NP40, and Halt protease inhibitor cocktail). After incubation for 15 min on a rotating wheel, the cell suspension was passed 10 times through a 21-gauge needle and centrifuged at 10,000 x g for 10 min, supernatants were collected. 1mg of proteins were incubated on a rotating wheel at room temperature for 1h with 25µl of magnetic anti-HA beads (Pierce). Beads were then washed four times in TBS-T (20mM Tris, 100mM NaCl, 0.05% Tween) and complexes were eluted in 30µl of RIPA buffer + 1% SDS. Eluates were denatured 30 min at 37°C in NuPAGE LDS sample buffer + NuPAGE reducing agent and were subjected to 3-8% Tris-Acetate gradient electrophoresis gel with Tris-Acetate running buffer with antioxidant reagent (Nupage system, Invitrogen), according to the manufacturer, and immunoblotted as described below. Input control for immunoprecipitation were performed on 30µg of HEK293 cell lysates, denatured 30 min at 37°C in NuPAGE LDS sample buffer + NuPAGE reducing agent and were subjected to 4-12% Bis-Tris gradient electrophoresis gels with MOPS running buffer (Nupage, Invitrogen), according to the manufacturer.

Immunoblots were performed as previously described using goat anti-AC8 (SantaCruz, SC-1967), mouse anti-HA (Abcam, ab-130275), and mouse anti beta-actin (Sigma-Aldrich, A5441) as primary antibodies and horseradish peroxidase (HRP)-conjugated anti-goat (Invitrogen, PA1-28664) and anti-mouse (BioRad,1706516) secondary antibodies. Immunolabeling was detected by enhanced

chemiluminescence using the Clarity western ECL substrate (BioRad), on ChemiDoc Imaging System (BioRad, Marnes-la-Coquette, France).

2.7 cAMP accumulation assay

cAMP accumulation in whole-cell lysates of transiently transfected HEK-293 cells was measured with the cAMP-Gs HiRange kit after incubation for 60 min with the PDE inhibitor IBMX (200 µM) and the general AC activator forskolin (fsk, 10 µM), according to the manufacturer's instructions.

2.8 Fluorescence microscopy

HEK cells were grown on 10mm poly-Lysine-coated coverslips and were transfected 24h with expressing vectors encoding HA-AC2, HA-AC3 or HA-AC6 with or without mGFP-AC8E or mGFP-AC8EΔNt. Cells were fixed by incubation with PBS containing 4% paraformaldehyde (PFA) for 10 min at 37°C. PFA was then neutralized by incubation for 10 min with PBS plus 50mM NH_4Cl at room temperature. Cells were permeabilized with 0.1% Triton X-100 for 15 min and blocked in 2% BSA for 60 min at room temperature. Cells were labelled with Alexa-596 conjugated anti-HA antibody (5 µg/mL in PBS + 0.1%BSA, Invitrogen #A21288) over night at 4°C. After 3 washes (PBS + 0.1%Tween20), coverslips were mounted with antifade Mounting Medium with DAPI (VectaShield H-1200-10). Images were acquired with a Leica SP5 confocal microscope (Leica Microsystems, Wetzlar, Germany).

2.9 cAMP imaging

Cells on 10mm poly-L-lysine-coated coverslips were transfected with the $^{T}Epac^{VV}$-encoding vector for 24 h. Coverslips were placed in a microscope chamber continually perfused (2 mL·min^{-1}) with BBS buffer (125mM NaCl, 2mM $CaCl_2$, 1mM $MgCl_2$, 1.25mM NaH_2PO_4, 26mM $NaHCO_3$, 25mM glucose) maintained at 32 °C and saturated with 95% O_2–5% CO_2. Ratiometric analyses were performed as follows:

fluorescence was excited with a LED source at 435 nm and fluorescence emission was monitored with a dichroic mirror (T450LPXR) and alternating emission filters for the donor (HQ480/40) and acceptor (D535/40). Pairs of images were recorded with an Orca-ER CCD camera (Hamamatsu Photonics, Japan), at 20-s intervals. Changes in $[cAMP]_i$ are expressed as the ratio of donor fluorescence (F480) to acceptor fluorescence (F535). The ratios were multiplied by the same constant for all experiments, such that the baseline ratio was 1 in basal conditions. The maximum ratio change (Rmax) was obtained by stimulating cells with 10 µM fsk and 200 µM IBMX. Filters and mirrors were obtained from AHF analysentechnik AG, Tübingen, Germany. Images were acquired with iVision (Biovision, Exton, PA, USA) and analyzed in the IGOR Pro environment (Wavemetrics, Lake Oswego, OR, USA) with a custom package, Ratioscope, available on a public data repository (DOI: 10.25493/5G5V-HBC). No correction for bleed-through or direct excitation of the acceptor was applied to keep the benefit of ratiometric cancellation of artifacts.

2.10 Statistics

All data are presented as the means ± SEM of at least three independent experiments. Meta-analysis of experiments was performed using the same Ratioscope package. The statistical significance of differences between groups was assessed with GraphPad Prism 6 (Graphpad Software Inc., La Jolla, CA, USA). The non-parametric two-tailed Mann-Whitney test was used for pairwise comparisons. The nonparametric two-tailed Kruskal-Wallis test and Dunn's post-test were used for multiple comparisons. Differences were considered significant if $P < 0.05$.

3. RESULTS

3.1 AC8E exerts a dominant-negative effect across AC families

AC8E exerts a dominant-negative effect on AC3 activity [9]. Therefore, we first tested whether AC8E could also exert a dominant-negative effect on other ACs such as AC2, from group 2, and, AC6, from group 3 (**Fig. 1**). Of note, AC6 is one of the two mostly expressed ACs in VSMCs, the other being AC3 [15,16]. Coimmunoprecipitation experiments (**Fig. 1A**) and cAMP accumulation assays (**Fig. 1B**) were performed on HEK-293 cells transiently expressing AC8E and/or HA-tagged AC2, AC3 or AC6 (HA-AC2; HA-AC3; HA-AC6). The expression of HA-tagged ACs and AC8E was confirmed by western blot (**Fig. 1A**, left panels).

After HA-immunoprecipitation of AC2, AC3 or AC6 (**Fig. 1A**, upper right panel), the anti-AC8 antibody revealed a single 115 kDa-band in HEK-293 cells co-expressing AC8E and HA-AC2, HA-AC3- or HA-AC6 (**Fig. 1A**, lower right panel, lanes 6, 7 and 8). Co-expression of AC8E with other AC significantly lowers levels of cAMP synthesis in response to fsk in cells co-expressing AC2, AC3, or AC6 and AC8E as compared to cells expressing full length ACs only (**Fig 1B**, AC8E/AC2 *vs* AC2: 221.7 ± 15.98 *vs* 627.0 ± 72.65%, $P<0.01$; AC8E/AC3 *vs* AC3: 121.0 ± 9.66 *vs* 326.0 ± 16.91%, $P<0.001$; AC8E/AC6 *vs* AC6: 363.1± 22.96 *vs* 629.3 ± 38.04%, $P<0.001$). AC8E alone also decreased the fsk-induced production of cAMP observed in pcDNA3 (control)-transfected cells suggesting that it dimerizes with endogenous ACs. Of note, AC2, AC3 and AC6 expressed alone are functional since fsk significantly raised cAMP accumulation (AC2 *vs* ctrl: 627.0 ± 72.65 *vs* 100.0 ± 6.72%, $P<0.01$; AC3 *vs* ctrl: 326.0 ±16.91 *vs* 100.0 ± 6.72%, $P<0.001$;AC6 *vs* ctrl: : 629.3 ± 38.04 *vs* 100.0 ± 6.72%, $P<0.001$). Altogether, these results suggest that AC8E

expression may constitute a broad system for negative regulation of the cAMP-dependent signal integration.

3.2 3D-structures of AC8 and AC8E.

To further explain the molecular dominant negative effect of AC8E, we used a homology modeling approach based on the 3D-structure of the bovine AC9 published by Qi et al [13]. These structural data were completed and refined as described in the Materials and Methods section in order to propose a predictive full structure of AC9 (**supplementary Fig. S1**), that served as a template for building predictive computational 3D models of full-length AC8A and truncated AC8E **(Fig. 2A** and **2B** left panels**)**. The position of the N-terminus domains of AC8A and AC8E (surface representation) and that of the adjacent transmembrane domains, TM1 for AC8A and TM6 for AC8E (cylindrical representation) are presented in **Fig. 2A** and **2B** right panels, respectively. Merging the surface representation of the two predicted 3D models of AC8A and AC8E (**Fig. 2C)** reveals that the lack of TM1-5 transmembrane domains in AC8E modifies the position of the TM6 domain (in orange) and consequently shifts the N-terminus of AC8E.

As mentioned by Qi et al [13], membrane domains can influence the catalytic domain *via* the helical domains (HD) and the adjacent coiled-coil regions, both defined for AC8A and AC8E in **supplementary Fig. S2**. We next identified the interactions between the N-terminus domain (referred to as SITE 1, **Table 1**) and the helical domains (HD1 and HD2) or the coiled-coil regions (referred to as SITE 2, **Table 1**), for both AC8A and AC8E. In AC8A, amino acids from the N-terminus domain form 6 hydrogen bonds with some of the HD1 domain residues and none involve the HD2 or coiled-coil regions (**Fig. 3A**). Conversely, in the AC8E, hydrogen bonds are predicted between the N-terminus domain and the coiled-coil regions, as well as between the

N-terminus domain and the HD2 domain (**Fig. 3B**). The molecular surface area volume (MSV) combined with the pocket molecular surface area (PMSA) highlighted 4 small cavity pockets (numbered 2, 16, 22, and 28) between the N-terminus and the coiled-coil region (H2.1) within the AC8E (**Fig. 3C**)**.** These small cavity pockets could reduce the flexibility of AC8E in the vicinity of the catalytic core and modify the shape and the structure of the protein. Thus, the analysis of AC8 predictive models shows that the missing part of AC8E (i.e.TM1-5) moves the AC8E N-terminus domain in a position that impacts the HDs orientation and coiled-coil regions.

3.3 The AC8E N-terminus domain is responsible for the inhibitory effect on AC partners.

Such a shift could possibly modify the catalytic core of AC heterodimers that include AC8E, and thus be involved in the AC8E-dominant negative effect [9]. To test whether the N-terminal domain is involved in the AC8E inhibitory effect on cAMP production, the amino acids from 2 to 179 were deleted. Before using this new construct, referred to as AC8EΔNt, we tested it for heterodimerization capacity and subcellular location compared to AC8E (**Fig. 4**). Co-immunoprecipitation studies were performed using the HA-antibody on lysates obtained from cells transiently expressing HA-tagged AC2, AC3 or AC6, with or without AC8E or AC8EΔNt (**Fig. 4A**). The expression of HA-AC2, HA-AC3, HA-AC6, AC8E and AC8EΔNt was confirmed by western blot (**Fig. 4A**, left panels). The analysis of HA-AC2, HA-AC3 and HA-AC6 immunoprecipitated complexes (**Fig 4A**, right panel lane 13 to 24) reveals a single band corresponding to AC8E (115 kDa) or AC8EΔNt (100 kDa) (**Fig. 4A** right panel, lane 19 to 24). No bands are observed in the negative control (**Fig.**

4A, right panel, lane 13). However, a low-intensity band is detected after HA-immunoprecipitation of HEK expressing AC8E or AC8EΔNt alone (**Fig. 4A**, right panel lane 14 and 15), resulting from non-specific interaction of the anti-HA antibody. Immunofluorescence experiments reveals that HA-AC2, HA-AC3 and HA-AC6 expressed alone, are mainly located at the plasma membrane (**Fig 4B**, lane 1,4 and 7), while they co-localized in intracellular compartments when co-expressed with AC8E or AC8EΔNt (**Fig 4B**, lane 2,5,8 and 3,6,9 respectively). AC8E and AC8EΔNt displayed a similar intracellular pattern of localization, in contrast to AC8 full-length (AC8A) which is at the plasma membrane (**Supplementary Figure S3.A**). This is consistent with our previous data demonstrating that AC8E is trapped inside the cell, while the functional full length AC8A is expressed at the plasma membrane [9]. Altogether, these results show that the deletion of the N-terminal domain of AC8E neither affects its subcellular location nor its ability to form heterodimers with AC2, AC3 and AC6.

cAMP dynamics and ACs functionality were measured in response to isoproterenol, an agonist selective of the Gs-protein coupled membrane β-adrenergic receptor (3nM) using the FRET-based biosensor $^{T}Epac^{VV}$ (**Fig. 5A and B**).). We used isolated clones of HEK cells stably expressing AC8E (HEK-AC8E clone #13) or AC8EΔNt (HEK-AC8EΔNt clone #6) selected for their similar levels of expression (**supplementary Fig. S3.B**). Of note, endogenous adenylyl cyclases transcripts expression was evaluated by real-time PCR in the HEK-293 cells used for this study (**supplementary Fig. S3.C**) and is quite similar to what has been described in the literature [17,18]. Relative changes in intracellular cAMP production in response to isoproterenol were monitored over time by calculating the ratio R of donor fluorescence emission (F480 nm) to acceptor (F535 nm) throughout the entire study.

Rmax was determined at the end of each experiment by adding 200 µM 3-isobutyl-1-methylxanthine (IBMX), a broad-spectrum PDE inhibitor, and 12 µM of fsk. For statistical analyses, cAMP level is systematically reported as a fraction of the maximum ratio change (Rmax), corresponding to saturation of the biosensor. As shown in **Fig. 5A and B**, the isoproterenol-induced cAMP signal in AC8EΔNt cells is not statistically different from in AC8E cells and both are significantly lower related to control cells (0.39 ± 0.05 fold of Rmax for AC8EΔNt and 0.37 ± 0.04 fold of Rmax for AC8E, and 0.59 ± 0.04 fold of Rmax for control**,** AC8EΔNt *vs* AC8E, P>0.99 n.s, AC8EΔNt *vs* control P<0.05, and AC8E *vs* control, P<0.05).

Over the past decade, the idea of GPCR signaling from intracellular membranes has gained ground [19,20]. A 2017 study, using conformational biosensors, even showed that β-1 adrenergic receptors localized in the Golgi are functional and capable of ligand binding, leading to cAMP production [21]. Since isoproterenol is a non permeant ligand, we revisited these experiments using forskolin (fsk), a cell permeant compound which activates all membrane-bound ACs, including intracellular membrane Acs (except AC9 that needs the presence of activated Gs), to determine whether or not the AC8E N-terminal domain is involved in inhibiting the cyclase activity of intracellular AC8E/ACs dimers (**Fig. 5C and D**). Consistently with our previous work [9]**,** the cAMP production in HEK-AC8E cells is lower in response to 5 µM fsk than in control cells (0.44 ± 0.05 *vs* 0.86 ± 0.03 fraction of Rmax**,** P<0.05**, Fig.5D**); conversely, that of HEK-AC8E∆Nt cells is similar to control HEK cells (0.91 ± 0.02 *vs* 0.86 ± 0.03 fraction of Rmax, ns, **Fig. 5D**). The baseline ratio and the Rmax were not significantly different between the different conditions **(Supplementary Fig.S4)**.

The global cell cyclase activity can be determined by measuring the slopes of traces while blocking phosphodiesterases (PDEs) [9]. To rule out any involvement of PDEs, we monitored cAMP synthesis over time in each cell in response to a low dose of fsk (1 µM) while blocking PDEs with 200 µM IBMX (**Fig. 5C** to **H**). In **Fig. 5E,** each colored thin trace represents the change in cAMP production within a single cell; the thick trace is the mean of all the traces obtained from a single experiment. **Fig. 5F** shows the average traces from 6 independent experiments obtained in response to 1µM fsk+IBMX. **Fig. 5G** recapitulates the mean of onset slopes calculated for each experiment. As shown in **Fig. 5F**, the average slope obtained from AC8E cells (magenta) is shallower than in control cells (black) whereas that of AC8E∆Nt (cyan) is similar. Accordingly, the average slope shows no statistical difference between AC8E∆Nt and control cells (2.99 ± 0.30 *vs* 2.49 ± 0.16, ns, **Fig. 5G**) conversely to that of AC8E cells which is significantly lower (1.17 ± 0.14 *vs* 2.49 ± 0.16**,** $p < 0.05$, **Fig. 5G**). Since the increase of the ratio depends on the buffering effect of the biosensor on cAMP -meaning that a slower onset is expected when the biosensor is present at a higher concentration-, we also plotted for each cell the slope at the origin of the ratio increase as a function of fluorescence intensity, used as a proxy for biosensor concentration **(Fig. 5H**). For the same amount of biosensor (or equal biosensor intensity expressed in count per second), the initial slope of the ratio curve (indicated by a symbol for each cell in **Fig. 5H**) is similar for AC8E∆Nt and control cells whereas lower in AC8E cells. These results demonstrate that the AC8E N-terminus domain is responsible for the inhibitory effect of AC8E on endogenous AC partners. Interestingly, partial deletions of the N-terminus domain (Δ2-44, Δ45-89, Δ90-134 and Δ135-179) did not prevent the AC8E dominant-negative effect

(**supplementary Fig. S5**), suggesting that it is triggered by the entire N-terminus domain rather than a particular motif.

Our results combined to previously published data [9,22,23] demonstrate that the dominant negative effect of AC8E is due to two domains i) the M2 domain, responsible for heterodimerization of AC8E/AC dimers, which should be involved in the entrapment of functional ACs inside the cell and, ii) the N-terminus domain inhibiting the catalytic core of AC8E/AC dimers. The trapping of AC8E/ACs dimers combined to the inhibitory effect of AC8E N-terminus domain on cAMP production prevents the integration of signals from the plasma and intracellular membranes (**Fig. 6**).

4. DISCUSSION

Here, we used template-based structure modeling [24] to predict the complete 3D structure of AC9 positioning the missing Nter and C1b domains [13]. Based on this, we then predicted the 3D models of the full-length AC8 (AC8A) and the truncated version AC8E by structural analysis with computational homological modeling, making this paper the first publication modeling the full 3D structures of two full-length ACs, AC8A and AC9. The comparative analysis of the AC8A and AC8E models combined with cAMP biosensor imaging of deletion mutants demonstrate that the AC8E N-terminal domain inhibits the AC activity of AC8E/ACs dimers.

The analysis of predicted structures revealed that the helical domains HD1 and HD2 are stabilized by coiled-coil regions next to the catalytic site ([13]**, Supplementary Fig. S2D**). Since coiled-coil domains are defined as "molecular rulers" for the assembly of the catalytic site of several enzymes [25–27], they likely provide the

framework for the correct dimerization of the C1a and C2a domains which together constitute the catalytic core. As a result of this, the N-terminal and C1b domains surrounding the helicoidal domains HD1 and HD2 (**Fig. 2 and Supplementary Fig. S2**) add a degree of constraint which undoubtedly contributes to the correct assembly of the catalytic site as suggested by Qi and coll [13].

In the AC8E, the lack of the transmembrane regions TM1-5 lead to several interdependent structural modifications. Indeed, the TM6 region changes position and becomes “perpendicular” to the M2 cassette; this translates into a drastic shift in the positioning of the N-terminus domain which, in turn, establishes new interactions towards coiled-coil regions leading to the formation of 4 small cavity pockets that likely destabilize HD1 and HD2 domains (**Fig. 2D**). Cavity pockets are known to modify local structure by decreasing protein packing densities of residues within helices [28]. As the possibly destabilized HD1 and 2 are in the vicinity of the catalytic core, one may assume that it changes the catalytic core structure of the AC dimers formed with AC8E, rendering the ensemble inactive. However, template-based modeling predicts the native structure of a protein target by sequence-sequence or sequence-structure alignment, but does not detail atomic interactions determining molecular structure [29]. Therefore, the assumption as to whether the cavity pockets effectively affect HD1 and HD2 structure and whether it destabilizes the catalytic core of the AC dimers formed with AC8E should be evaluated using molecular dynamics combined with molecular docking within a lipid bilayer.

According to structural data suggesting that the dominant-negative effect of AC8E on AC partners comes from its N-terminus domain, deleting it prevents the decrease of cAMP production in response to forskolin (**Fig. 5D**). However, we also found that this did not occur with the selective β-adrenergic membrane receptor agonist isoproterenol (**Fig. 5B**) due to AC8EΔNt intracellular location (**Fig. 4B and S3A**). The

intracellular AC8EΔNt remains able to dimerize with AC partners (**Fig. 4A**), preventing the export of AC8EΔNt-AC dimers towards the plasma membrane. Thus, one may suggest that the N-terminus domain is involved in both the dominant-negative effect and intracellular localization of AC8E. In support of such an assumption, the targeting of the full-length AC8 to the plasma membrane depends on the binding of caveolin1 to two "caveolin-binding motifs," CBM1 and CBM2 localized in the N- and C-terminal domains, respectively [30].

The intracellular retention of ACs heterodimers by AC8E is one of the mechanisms for regulating the integration of extracellular signals mediated by plasma membrane G protein-coupled receptors. In this respect, the AC8E is one more example of truncated transmembrane proteins acting in a dominant-negative manner by retaining their functional homologue inside the cells in the ER [31–37]. However, the central concept that signaling through second messengers such as cAMP takes place only at the plasma membrane is increasingly being questioned since functionally relevant GPCR and AC isoforms have been found in intracellular compartments such as endosomes, ER and golgi vesicles [21,38,39]. Bearing this in mind, the AC8E N-terminus-dependent mechanism of regulation of cAMP signaling takes on a new dimension, although functional ACs in ER have been poorly documented.

Alternate splicing of several ACs mRNA naturally occurs in different tissues and species, including humans [18,40–42] (Genbank AB007882, AA961399, AW002651, AW969619, AI807304, BE466682, AV723967). Expression of short ACs issued from mRNA spliced variants combined with heterodimerization process could therefore constitute a general system of regulation for the signal transduction involving cAMP-dependent pathways. This idea strengthens the case for characterizing the patterns

of expression of AC splice variants as well as the subcellular location, the function and the pathophysiological implications of their corresponding proteins.

FIGURES LEGENDS

Figure 1. AC8E interacts with AC2, AC3 and AC6 and exerts a dominant negative effect on their activitiy.

A. Western Blots. **Left panels :** Input showing the levels of expression of AC2, AC3 , AC6, AC8E and β-actin in HEK-293 cells transiently transfected. **Right panels:** immunoblots (IB) with AC8 antibody (*lower panel*) and HA-antibody (*upper panel*) after HA-immunoprecipitation (IP). Blot presented are representative of 4 independent experiments.

B. cAMP accumulation assay performed on HEK293 cells transiently expressing AC8E and/or AC2, AC3 or AC6, after a 60-min treatment with forskolin (10μM) in the presence of IBMX (200μM). The results are expressed in % of control cells and are represented as mean ± SEM of 4-9 independent experiments**.** Statistical analysis was carried out with the Mann-Whitney nonparametric test. *** P <0.001, ** P <0.01 compared to control cells; $^{###}$ P <0.001, $^{\#}$ P <0.05 compared to the corresponding full AC expressed alone.

Figure 2. Predictive 3D complete models of adenylyl cyclase 8A and 8E reveal change in N-terminal domain positioning.

Predictive 3D-structure of *Rattus norvegicus* full-length AC8A (**A**) and truncated AC8E (**B**). *Left Panels:* The C1b (blue) and N-terminal (green) domains are parallel and both surround the helical domains (HD1 and HD2, in red). *Right panels*: Overall structures of the AC8A and AC8E models in a ribbon representation. The N-domains of AC8A (blue), and AC8E (olive green) are shown using surface representation. The TM1 in AC8A and TM6 in AC8E are represented in green and orange cylindrical cartoons, respectively. ***C.*** *Left:* Superimposition of the AC8A and AC8E predictive

3D-structures. *Right.* 180° z-rotation. The shift of the Nter domain of AC8E is indicated by a dashed arrow.

Figure 3. Interactions between N-domain and coiled-coil regions differ from AC8A and AC8E.

Identification of the interaction sites between the N-domain and coiled-coil regions in full length AC8A (**A**) and truncated AC8E (**B**). The amino acids of HD domains or coiled-coil regions for both AC8A and AC8E are given in red; that of the N-terminus domain of AC8A and AC8E are given in blue and green, respectively.

Representation of the four cavity pockets identified in AC8E formed by the interaction sites between the N-domain and H2.1 coiled-coil region (**C**). Detailed information is given in **Table 1** for each interaction. Red helix: Coiled-coil region (H2.1); Green loop: part of N-domain; Grey surface: interaction site/pocket.

Figure 4. **Deletion of AC8E N-terminus domain does not affect its ability to interact with AC2, AC3 or AC6, neither intracellular retention of other ACs.**

A. Western Blots. **Left panels :** Input showing the levels of expression of HA-AC2, HA-AC3 , HA-AC6, AC8E, AC8EΔNt and β-actin in HEK-293 cells transiently transfected. **Right panels:** immunoblots (IB) with AC8 antibody (*upper panel*) and HA-antibody (*lower panel*) after HA-immunoprecipitation (IP). Membranes were incubated first with anti-AC8 R20 antibody, then stripped to be blotted with HA antibody. Asterisk represent remaining AC8 signal on HA-blotted membranes. Blots presented are representative of 2 independent experiments.

B. Subcellular localization of AC8E, AC8EΔNt, AC2, AC3 and AC6. HEK were transfected with HA-AC2, HA-AC3, HA-AC6 with or without AC8E-mGFP, or

AC8EΔNt-mGFP encoding vectors. Confocal images were acquired with a Leica SP5 confocal microscope (63x). Scale bar =20µm.

Figure 5: **Deletion of AC8E N-terminus domain restores cAMP production in response to isoproterenol, but not to forskolin.**

Cyclic cAMP production induced by isoproterenol (**A** and **B)** or forskolin (**C** to **H**) in HEK cells stably expressing pcDNA3 (control), pcDNA3-AC8E (AC8E) or pcDNA3-AC8EΔNt (AC8EΔNt).

Panels A and C.*Top panels***:** microscopy fields in grayscale (top left) show biosensor fluorescence at 535 nm. The F480/F535 ratio is determined for individual cells, within regions of interest (ROIs) delimited with colored contours. The calibration square indicates the range of intensity (in counts/pixel/s) horizontally and the F480/F535 ratio vertically. Pseudocolored images represent the F480/F535 ratio indicating the [cAMP]i (a) before treatment, (b) during stimulation with 3nM isoproterenol (**panel A**) or 5µM forskolin (**panel C**) and (c) during the application of fsk (12 µM) + IBMX (200µM), corresponding to the maximal ratio change (Rmax). *Bottom panels***:** each thin trace indicates the F480/F535 emission ratio over time in individual cells. The thick line represents the average of all traces. **Panels B and D**. Dot plot and bars representing the mean values for isoproterenol-induced (**panel B**) or fsk-induced (**panel D**) cAMP production are expressed in fraction of the maximal ratio (Rmax) change. Data shown are the means ± SEM of N=6 to 7 independent experiments. For each independent experiment, the symbol represents the mean of n=10 to 30 individual cells. Multiple comparisons were performed with the Kruskal-Wallis test. *: P <0.05, **: P <0.01, ns: not significant. **Panels E-H.** Biosensor imaging for measuring the onset slopes corresponding to global cyclase activity in cells. Fast bath application of a low concentration of fsk (1µM) moderately activated ACs while

cAMP degradation by PDEs was blocked with IBMX (200 µM). For each cell, biosensor concentration was estimated by measuring the intensity of the 10% brightest pixels within the region of interest. **E.** The color code of each ROI (**top panels**) reflects biosensor concentration: from blue (low concentration) to red (high concentration); matching color thin traces (**bottom panels**) indicate the F480/F535 emission ratio over time in the ROIs delimiting each cell. The thick trace represents the mean recordings. **F.** Average traces in response to 1µM fsk + 200µM IBMX are calculated based on the mean (thick) traces from 6 independent experiments. Shading indicates 95% confidence interval. **G.** Mean of onset slopes calculated for each independent experiment (N=6 per condition). **H.** Onset slope of the fluorescence ratio for each cell plotted against fluorescence intensity (reflecting biosensor expression levels). Results of only 3 out of 6 independent experiments are shown for a better readability.

Figure 6: Cartoon of the AC8E-dependent inhibitory mechanism on cAMP production.

Top Panel. Integration of extracellular signals mediated by G proteins-coupled receptors leading to cyclic AMP production at plasma and intracellular membranes. **Bottom Panel.** AC8E-dependent inhibitory mechanisms on cAMP production.

Table

Table 1. The list of individual interactions identified between N and helical domains of adenylate cyclase AC8A and AC8E models (SITE1=N-terminus domain, SITE2 = HD1, HD2, coiled-coil regions). #:number of poses for each AC. NR* (neighbor residues) = Amino-Acids closed to the h2.1 region.

#	Models	Site 1		Site 2		Interaction	Distance (Å)
1	**AC8A**	Gly57	N	Arg341	HD1	Hydrogen	3.11
2	**AC8A**	Tyr167	N	Arg344	HD1	Hydrogen	3.17
3	**AC8A**	Glu164	N	Arg344	HD1	Hydrogen	3.05
4	**AC8A**	Gly58	N	Gln345	HD1	Hydrogen	3.03
5	**AC8A**	Asn156	N	Arg351	HD1	Hydrogen	2.76
6	**AC8A**	Gln14	N	Arg359	HD1	Hydrogen	3.10
1	**AC8E**	His128	N	Arg206	HD1	Hydrogen	3.26
2	**AC8E**	Ser116	N	Asp785	HD2	Hydrogen	2.81
3	**AC8E**	Asn67	N	Arg803	h2.1	Hydrogen	3.06
4	**AC8E**	Asn67	N	Glu807	h2.1	Hydrogen	3.11
5	**AC8E**	His52	N	Arg811	h2.1NR*	Hydrogen	3.31
6	**AC8E**	Arg55	N	Glu824	h2.2	Hydrogen	2.74

SUPPLEMENTARY FIGURES LEGENDS

Supplementary Figure S1. Putative complete structure of adenylyl cyclase 9.

A. The complete structure of *Bos taurus* AC9 including the missing N-terminal, C1b, and C2b domains and the loop regions. **B.** The orientation of the C1b domain (blue) is highlighted in mesh representation (grey). The C1b domain connects together the C1a and TM7 domains. **C.** Representation of AC9 3D model turned forward by 90°. The C1b (blue) and N-terminal (green) domains are paralleled and both surround the helical domains (HD1 and HD2, in red). **D**. The coiled-coil regions of AC9 (h1.1 -

cyan, h1.2 - grey, h2.1- yellow, and h2.2 - green) stabilizing the HD1 and HD2 as mentioned by Qi et al. 2019, are shown with cartoon stick representation [12].

The newly incorporated N-terminus and C2B domains are linked to the N-terminal region of the TM1 helix and the C-terminal of C2A, respectively. The C1B domain parallels the N-domain based on docking results. Considering the orientation of the N and C1B domains, they twist around the helical parts HD1 and HD2, respectively. These observations correlate the unresolved density maps of both N-terminal and C1B domains of AC9 [12].

Supplementary Figure S2. Coiled-coil regions of AC8A and AC8E.

AC8A and AC8E coiled-coil regions were identified by multiple sequence alignment with the coiled-coil region of AC9 (h1.1, h1.2, h2.1 and h2.2 are highlighted in bold and underlined).

Supplementary Figure S3. Characterization of AC8E and AC8EΔNt expression in HEK-transfected and expression level of ACs transcripts in HEK.

A. Subcellular localization of AC8A (as a control of Adenylyl cyclase localization at plasma membrane), AC8E or AC8EΔNt. HEK were transfected with AC8A-mGFP, AC8E-mGFP, or AC8EΔNt-mGFP encoding vectors. Confocal images were acquired with a Leica SP5 confocal microscope (63x). Scale bar = 20µm. **B.** Western Blots showing the levels of expression of AC8E or AC8EΔNt in monoclonal stable HEK-293 obtained by limiting dilution. Immunoblots (IB) with AC8 antibody (*upper panel*) and beta actin-antibody (*lower panel*). Immunoblots were performed twice. **C.** Endogenous adenylyl cyclases transcripts in HEK-293 cell line, normalized to HPRT.

n.d: not detected (Cp>33). RT-qPCR were performed as preciously described by Vallin et al [9], primers used are presented in supplementary table S2. The results represent the mean ± SEM of 4 independent experiments.

Supplementary Figure S4. Basal and maximal cAMP levels in HEK.

Baseline ratio (referred as R basal) and maximal ratio (Rmax) in HEK-293 cells stably expressing empty vector (ctrl), AC8E or AC8EΔNt in biosensors experiments for measuring cAMP production in response to isoproterenol (A) or forskolin (B) . The data are the means ± SD of N=7 (**A**) or N=6 (**B**) independent experiments. For each independent experiment, values used represent the mean of n= 10 to 30 individual cells. The nonparametric two-tailed Kruskal-Wallis test awas used, P values are given on the graph.

Supplementary Figure S5. Iterative deletions of 45aa within AC8E N-terminal do not restore cAMP production.

A. cAMP accumulation assays on HEK cells transfected with empty vector (control), AC8E-; AC8EΔNt-; AC8EΔ2-44-; AC8EΔ45-89-; AC8EΔ90-135- or AC8EΔ135-179-encoding vectors after 1 hour of fsk (10µM) +IBMX (500µM) treatment. Results are expressed in % of control and the means ± SEM of 3 independent experiments are shown. Values were as follows: for Ctrl : 100,0 ± 0,00 % ; AC8E : 28,06 ± 3,61 % ; AC8EΔNt : 110,9 ± 5,77 % ; AC8EΔ2-44 : 36,50 ± 5,71 % ; AC8EΔ45-89 : 31,79 ± 1,38 % ; AC8EΔ90-135 : 32,83 ± 5,15 % ; AC8EΔ135-179 : 61,77 ± 9,49 %. Side-by-side comparisons were performed with the Kruskal-Wallis test for unpaired data. **: P<0.01, ns : not significant. **B.** Immunoblot showing the levels of expression of AC8E, AC8EΔNt,

AC8E∆2-44; AC8E∆45-89; AC8E∆90-135, AC8E∆135-179 and β-actin in HEK-293 cells transiently transfected.

Supplementary Table 1: Cloning primers and strategies.

Supplementary table 2: List of primers used for RT-qPCR.

Acknowledgements:

We would like to thank JF. Gilles from the imaging facility of the Paris-Seine Biological Institute (IBPS), C. Dessauer for providing the AC3, AC2 and AC6 constructs and JB. Klarenbeek for providing the $^{T}Epac^{VV}$ expression plasmid.

This work was supported by the French Federation of Cardiology (FFC), the *Nouvelle Société Francophone d'Athérosclérose* (NSFA), the *Société Française de Cardiologie* (SFC), the *Groupe de Réflexion sur la Recherche Cardiovasculaire* (GRRC), the *Fondation de France* (FDF) and the chair of research in molecular modeling MAgICS.

REFERENCES

[1] N. Defer, M. Best-Belpomme, J. Hanoune, Tissue specificity and physiological relevance of various isoforms of adenylyl cyclase., Am J Physiol Renal Physiol. 279 (2000) F400-16. https://doi.org/10.1152/ajprenal.2000.279.3.F400.

[2] R.K. Sunahara, C.W. Dessauer, A.G. Gilman, Complexity and diversity of mammalian adenylyl cyclases., Annu Rev Pharmacol Toxicol. 36 (1996) 461–80. https://doi.org/10.1146/annurev.pa.36.040196.002333.

[3] W.J. Tang, M. Stanzel, A.G. Gilman, Truncation and alanine-scanning mutants of type I adenylyl cyclase., Biochemistry. 34 (1995) 14563–72. https://doi.org/10.1021/bi00044a035.

[4] J.J. Tesmer, R.K. Sunahara, A.G. Gilman, S.R. Sprang, Crystal structure of the catalytic domains of adenylyl cyclase in a complex with Gsalpha.GTPgammaS., Science. 278 (1997) 1907–16. https://doi.org/10.1126/science.278.5345.1907.

[5] G. Zhang, Y. Liu, A.E. Ruoho, J.H. Hurley, Structure of the adenylyl cyclase catalytic core., Nature. 386 (1997) 247–53. https://doi.org/10.1038/386247a0.

[6] S.C. Van Keulen, D. Narzi, U. Rothlisberger, Association of Both Inhibitory and Stimulatory Gα Subunits Implies Adenylyl Cyclase 5 Deactivation, Biochemistry. 58 (2019) 4317–4324. https://doi.org/10.1021/acs.biochem.9b00662.

[7] D.M. Cooper, A.J. Crossthwaite, Higher-order organization and regulation of adenylyl cyclases., Trends Pharmacol Sci. 27 (2006) 426–31. https://doi.org/10.1016/j.tips.2006.06.002.

[8] A. Baragli, M.L. Grieco, P. Trieu, L.R. Villeneuve, T.E. Hébert, Heterodimers of adenylyl cyclases 2 and 5 show enhanced functional responses in the presence of Galpha s., Cell Signal. 20 (2008) 480–92. https://doi.org/10.1016/j.cellsig.2007.10.033.

[9] B. Vallin, Y. Legueux-Cajgfinger, N. Clément, M. Glorian, L. Duca, P. Vincent, I. Limon, R. Blaise, Novel short isoforms of adenylyl cyclase as negative regulators of cAMP production, Biochim Biophys Acta Mol Cell Res. 1865 (2018) 1326–1340. https://doi.org/10.1016/j.bbamcr.2018.06.012.

[10] J.J. Cali, R.S. Parekh, J. Krupinski, Splice variants of type VIII adenylyl cyclase. Differences in glycosylation and regulation by Ca2+/calmodulin., J Biol Chem. 271 (1996) 1089–95. https://doi.org/10.1074/jbc.271.2.1089.

[11] N. Defer, O. Marinx, D. Stengel, A. Danisova, V. Iourgenko, I. Matsuoka, D. Caput, J. Hanoune, Molecular cloning of the human type VIII adenylyl cyclase., FEBS Lett. 351 (1994) 109–13. https://doi.org/10.1016/0014-5793(94)00836-1.

[12] D. Delmeire, D. Flamez, S.A. Hinke, J.J. Cali, D. Pipeleers, F. Schuit, Type VIII adenylyl cyclase in rat beta cells: coincidence signal detector/generator for glucose and

GLP-1., Diabetologia. 46 (2003) 1383–93. https://doi.org/10.1007/s00125-003-1203-8.

[13] C. Qi, S. Sorrentino, O. Medalia, V.M. Korkhov, The structure of a membrane adenylyl cyclase bound to an activated stimulatory G protein., Science. 364 (2019) 389–394. https://doi.org/10.1126/science.aav0778.

[14] L.A. Kelley, S. Mezulis, C.M. Yates, M.N. Wass, M.J. Sternberg, The Phyre2 web portal for protein modeling, prediction and analysis., Nat Protoc. 10 (2015) 845–58. https://doi.org/10.1038/nprot.2015.053.

[15] R.S. Ostrom, X. Liu, B.P. Head, C. Gregorian, T.M. Seasholtz, P.A. Insel, Localization of adenylyl cyclase isoforms and G protein-coupled receptors in vascular smooth muscle cells: expression in caveolin-rich and noncaveolin domains., Mol Pharmacol. 62 (2002) 983–92. https://doi.org/10.1124/mol.62.5.983.

[16] J.G. Webb, P.W. Yates, Q. Yang, Y.V. Mukhin, S.M. Lanier, Adenylyl cyclase isoforms and signal integration in models of vascular smooth muscle cells., Am J Physiol Heart Circ Physiol. 281 (2001) H1545-52. https://doi.org/10.1152/ajpheart.2001.281.4.H1545.

[17] K. Lefkimmiatis, M. Srikanthan, I. Maiellaro, M.P. Moyer, S. Curci, A.M. Hofer, Store-operated cyclic AMP signalling mediated by STIM1, Nat Cell Biol. 11 (2009) 433–442. https://doi.org/10.1038/ncb1850.

[18] M.G. Ludwig, K. Seuwen, Characterization of the human adenylyl cyclase gene family: cDNA, gene structure, and tissue distribution of the nine isoforms., J Recept Signal Transduct Res. 22 (2002) 79–110. https://doi.org/10.1081/rrs-120014589.

[19] S.E. Crilly, M.A. Puthenveedu, Compartmentalized GPCR Signaling from Intracellular Membranes., J Membr Biol. 254 (2021) 259–271. https://doi.org/10.1007/s00232-020-00158-7.

[20] A. Radoux-Mergault, L. Oberhauser, S. Aureli, F.L. Gervasio, M. Stoeber, Subcellular location defines GPCR signal transduction., Sci Adv. 9 (2023) eadf6059. https://doi.org/10.1126/sciadv.adf6059.

[21] R. Irannejad, V. Pessino, D. Mika, B. Huang, P.B. Wedegaertner, M. Conti, M. von Zastrow, Functional selectivity of GPCR-directed drug action through location bias., Nat Chem Biol. 13 (2017) 799–806. https://doi.org/10.1038/nchembio.2389.

[22] C. Gu, A. Sorkin, D.M. Cooper, Persistent interactions between the two transmembrane clusters dictate the targeting and functional assembly of adenylyl cyclase, Curr Biol. 11 (2001) 185–90.

[23] C. Gu, J.J. Cali, D.M. Cooper, Dimerization of mammalian adenylate cyclases., Eur J Biochem. 269 (2002) 413–21.

[24] A. Szilagyi, Y. Zhang, Template-based structure modeling of protein–protein interactions, Current Opinion in Structural Biology. 24 (2014) 10–23.

https://doi.org/10.1016/j.sbi.2013.11.005.

[25] G. Hagelueken, B.R. Clarke, H. Huang, A. Tuukkanen, I. Danciu, D.I. Svergun, R. Hussain, H. Liu, C. Whitfield, J.H. Naismith, A coiled-coil domain acts as a molecular ruler to regulate O-antigen chain length in lipopolysaccharide., Nat Struct Mol Biol. 22 (2015) 50–56. https://doi.org/10.1038/nsmb.2935.

[26] L. Truebestein, D.J. Elsner, E. Fuchs, T.A. Leonard, A molecular ruler regulates cytoskeletal remodelling by the Rho kinases., Nat Commun. 6 (2015) 10029. https://doi.org/10.1038/ncomms10029.

[27] L. Truebestein, T.A. Leonard, Coiled-coils: The long and short of it., Bioessays. 38 (2016) 903–16. https://doi.org/10.1002/bies.201600062.

[28] S. Sonavane, P. Chakrabarti, Cavities and atomic packing in protein structures and interfaces., PLoS Comput Biol. 4 (2008) e1000188. https://doi.org/10.1371/journal.pcbi.1000188.

[29] H. Geng, F. Chen, J. Ye, F. Jiang, Applications of Molecular Dynamics Simulation in Structure Prediction of Peptides and Proteins., Comput Struct Biotechnol J. 17 (2019) 1162–1170. https://doi.org/10.1016/j.csbj.2019.07.010.

[30] V.G. Tabbasum, D.M.F. Cooper, Structural and Functional Determinants of AC8 Trafficking, Targeting and Responsiveness in Lipid Raft Microdomains., J Membr Biol. 252 (2019) 159–172. https://doi.org/10.1007/s00232-019-00060-x.

[31] M. Benkirane, D.Y. Jin, R.F. Chun, R.A. Koup, K.T. Jeang, Mechanism of transdominant inhibition of CCR5-mediated HIV-1 infection by ccr5delta32., J Biol Chem. 272 (1997) 30603–6. https://doi.org/10.1074/jbc.272.49.30603.

[32] M. De Bellis, F. Pisani, M.G. Mola, D. Basco, F. Catalano, G.P. Nicchia, M. Svelto, A. Frigeri, A novel human aquaporin-4 splice variant exhibits a dominant-negative activity: a new mechanism to regulate water permeability., Mol Biol Cell. 25 (2014) 470–80. https://doi.org/10.1091/mbc.E13-06-0331.

[33] R. Grosse, T. Schöneberg, G. Schultz, T. Gudermann, Inhibition of gonadotropin-releasing hormone receptor signaling by expression of a splice variant of the human receptor., Mol Endocrinol. 11 (1997) 1305–18. https://doi.org/10.1210/mend.11.9.9966.

[34] K.D. Karpa, R. Lin, N. Kabbani, R. Levenson, The dopamine D3 receptor interacts with itself and the truncated D3 splice variant d3nf: D3-D3nf interaction causes mislocalization of D3 receptors., Mol Pharmacol. 58 (2000) 677–83. https://doi.org/10.1124/mol.58.4.677.

[35] J. Rhyne, M.M. Mantaring, D.F. Gardner, M. Miller, Multiple splice defects in ABCA1 cause low HDL-C in a family with hypoalphalipoproteinemia and premature coronary disease., BMC Med Genet. 10 (2009) 1. https://doi.org/10.1186/1471-2350-10-1.

[36] C.L. Wellington, Y.Z. Yang, S. Zhou, S.M. Clee, B. Tan, K. Hirano, K. Zwarts, A.

Kwok, A. Gelfer, M. Marcil, S. Newman, K. Roomp, R. Singaraja, J. Collins, L.H. Zhang, A.K. Groen, K. Hovingh, A. Brownlie, S. Tafuri, J. Genest, J.J. Kastelein, M.R. Hayden, Truncation mutations in ABCA1 suppress normal upregulation of full-length ABCA1 by 9-cis-retinoic acid and 22-R-hydroxycholesterol., J Lipid Res. 43 (2002) 1939–49. https://doi.org/10.1194/jlr.m200277-jlr200.

[37] X. Zhu, J. Wess, Truncated V2 vasopressin receptors as negative regulators of wild-type V2 receptor function., Biochemistry. 37 (1998) 15773–84. https://doi.org/10.1021/bi981162z.

[38] D. Calebiro, V.O. Nikolaev, M.C. Gagliani, T. de Filippis, C. Dees, C. Tacchetti, L. Persani, M.J. Lohse, Persistent cAMP-signals triggered by internalized G-protein-coupled receptors., PLoS Biol. 7 (2009) e1000172. https://doi.org/10.1371/journal.pbio.1000172.

[39] R.S. Ostrom, A.S. Bogard, R. Gros, R.D. Feldman, Choreographing the adenylyl cyclase signalosome: sorting out the partners and the steps., Naunyn Schmiedebergs Arch Pharmacol. 385 (2012) 5–12. https://doi.org/10.1007/s00210-011-0696-9.

[40] G. Iwami, M. Akanuma, J. Kawabe, P.J. Cannon, C.J. Homcy, Y. Ishikawa, Multiplicity in type V adenylylcyclase: type V-a and type V-b., Mol Cell Endocrinol. 110 (1995) 43–7. https://doi.org/10.1016/0303-7207(95)03514-8.

[41] S. Katsushika, J. Kawabe, C.J. Homcy, Y. Ishikawa, In vivo generation of an adenylylcyclase isoform with a half-molecule motif., J Biol Chem. 268 (1993) 2273–6.

[42] J. Wallach, M. Droste, F.W. Kluxen, T. Pfeuffer, R. Frank, Molecular cloning and expression of a novel type V adenylyl cyclase from rabbit myocardium., FEBS Lett. 338 (1994) 257–63. https://doi.org/10.1016/0014-5793(94)80279-3.

A

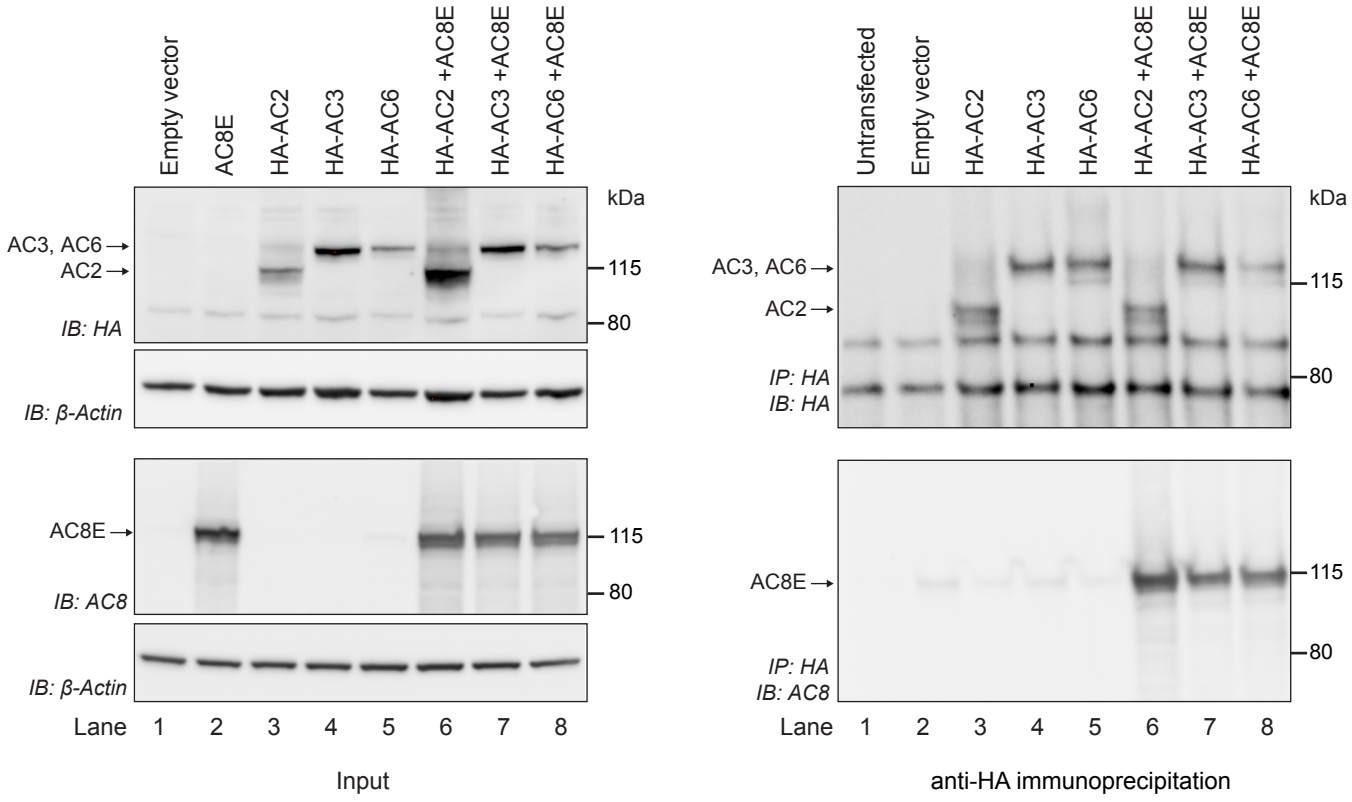
Empty vector
AC8E
HA-AC2
HA-AC3
HA-AC6
HA-AC2 +AC8E
HA-AC3 +AC8E
HA-AC6 +AC8E
kDa
AC3, AC6
AC2
IB: HA
IB: β-Actin
AC8E
IB: AC8
115
80
Lane 1 2 3 4 5 6 7 8
Input
Untransfected
IP: HA
IB: HA
IP: HA
IB: AC8
anti-HA immunoprecipitation

B

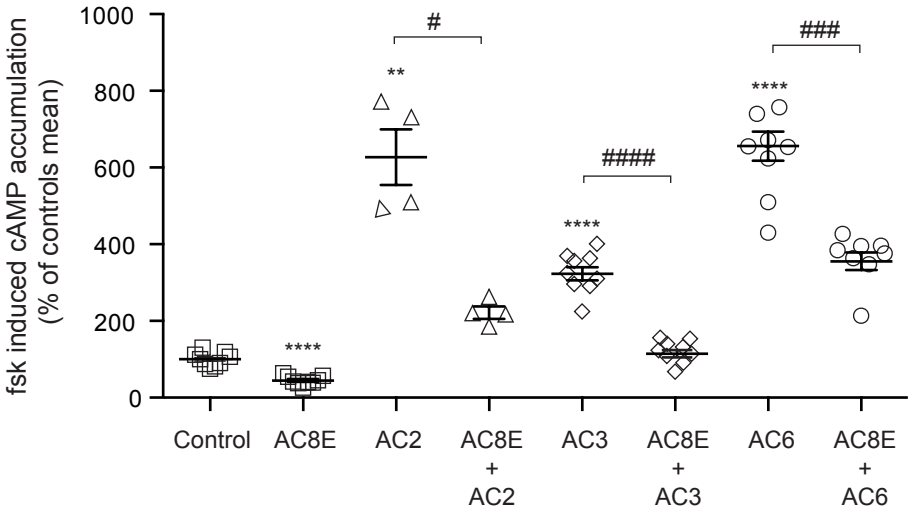
fsk induced cAMP accumulation
(% of controls mean)
1000
800
600
400
200
0
#
###
####
**
****
Control
AC8E
AC2
AC8E + AC2
AC3
AC8E + AC3
AC6
AC8E + AC6

Figure 1

A Full-length AC8A

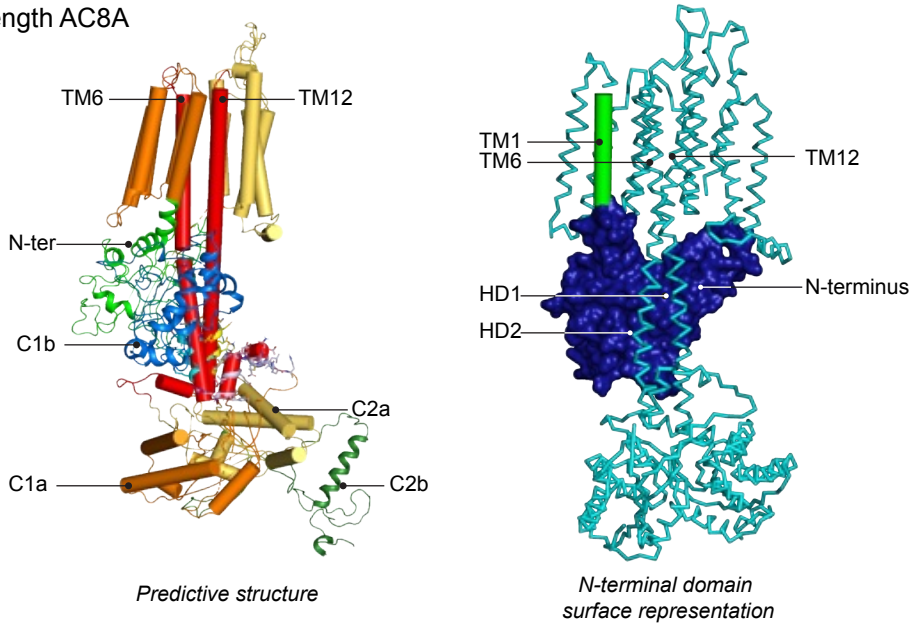

Predictive structure

N-terminal domain surface representation

B Truncated AC8E

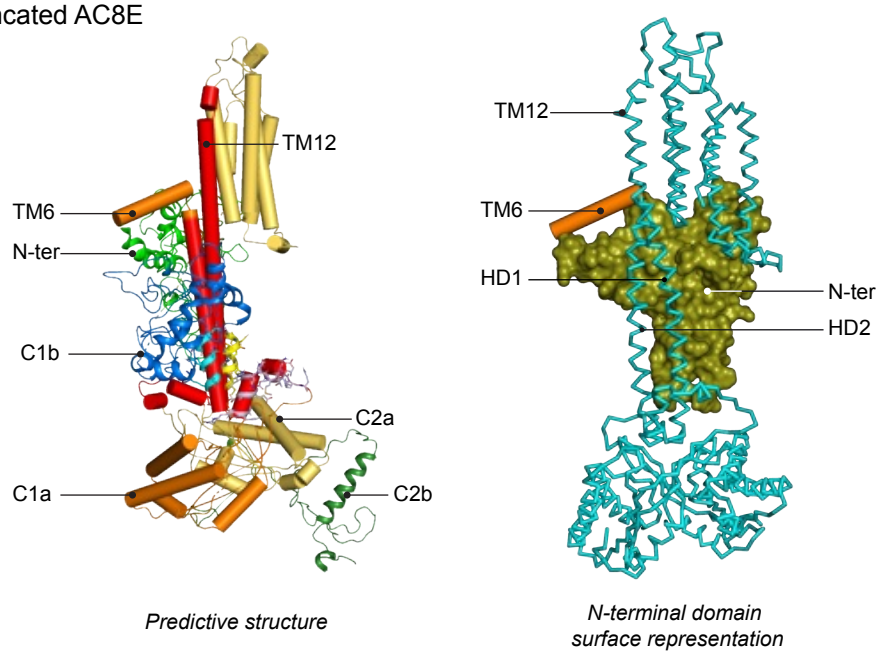

Predictive structure

N-terminal domain surface representation

C AC8A/AC8E Models superimposition

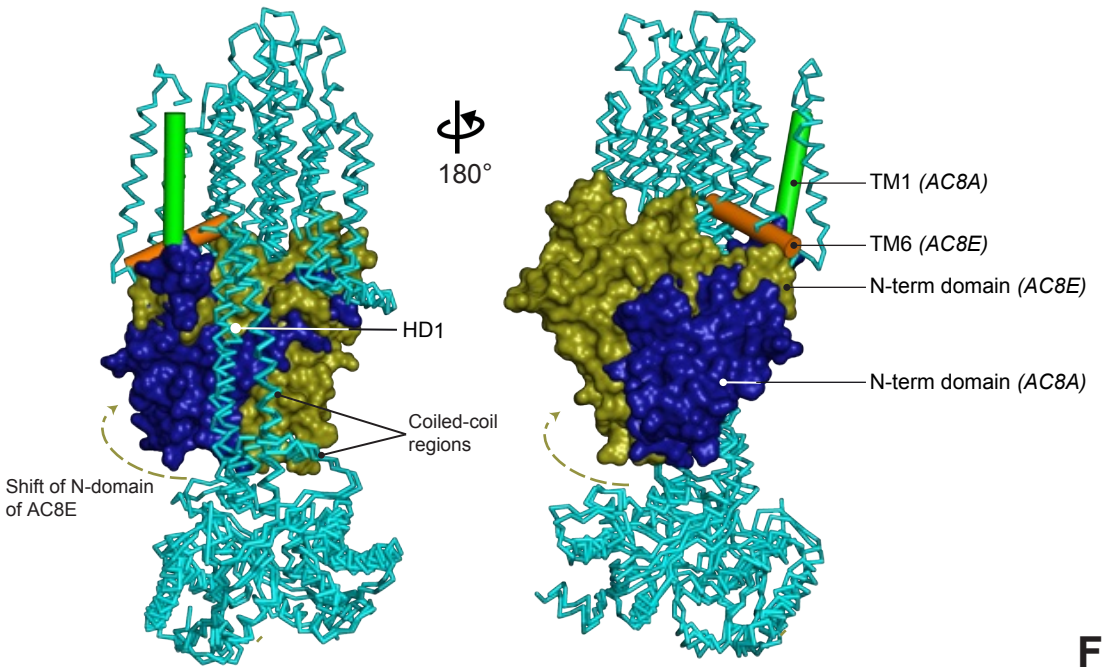

Figure 2

A Full-length AC8A

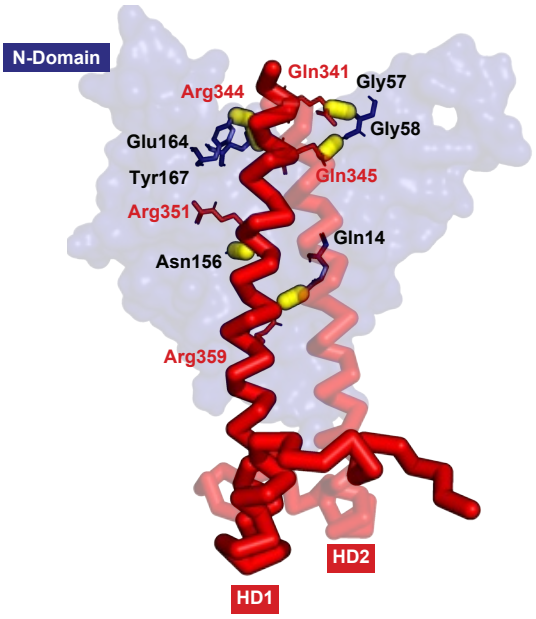

B Truncated AC8E

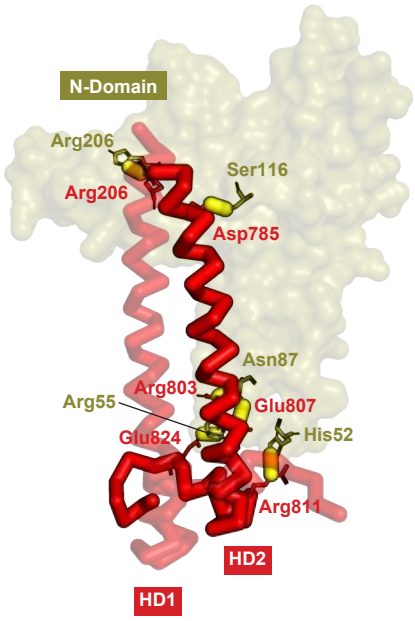

C Truncated AC8E cavity pockets

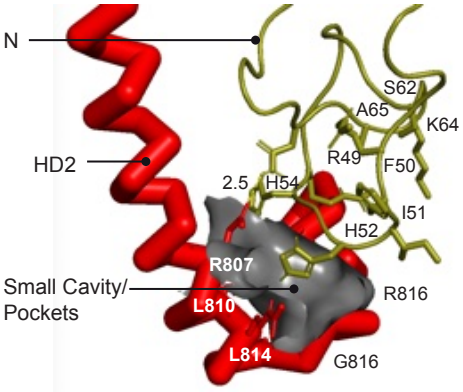

Pocket Id 2

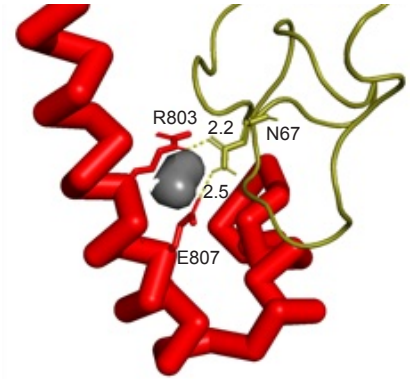

Pocket Id 16

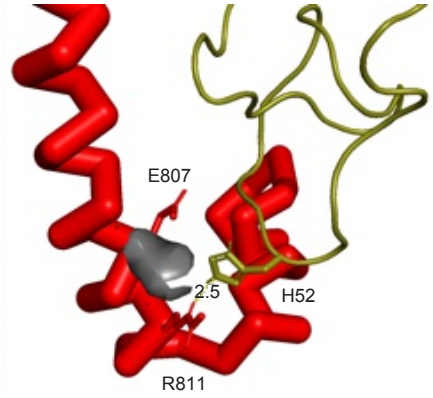

Pocket Id 22

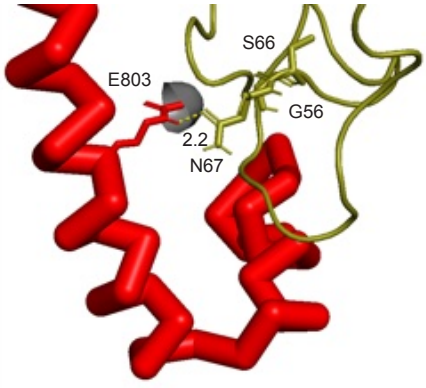

Pocket Id 28

Figure 3

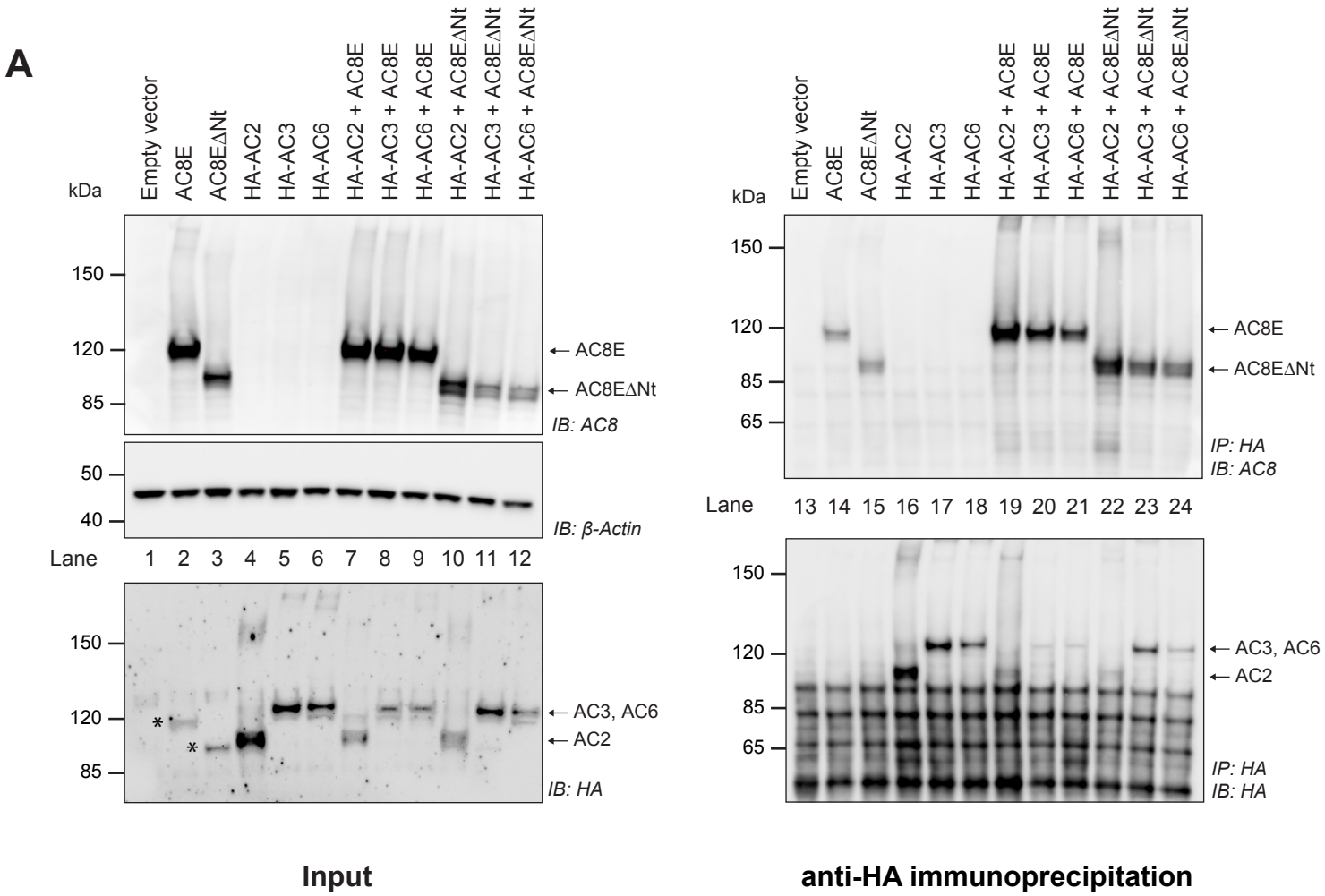
A
Empty vector
AC8E
AC8EΔNt
HA-AC2
HA-AC3
HA-AC6
HA-AC2 + AC8E
HA-AC3 + AC8E
HA-AC6 + AC8E
HA-AC2 + AC8EΔNt
HA-AC3 + AC8EΔNt
HA-AC6 + AC8EΔNt
kDa
150
120
85
50
40
← AC8E
← AC8EΔNt
IB: AC8
IB: β-Actin
Lane 1 2 3 4 5 6 7 8 9 10 11 12
← AC3, AC6
← AC2
IB: HA
Lane 13 14 15 16 17 18 19 20 21 22 23 24
65
IP: HA
IB: AC8
IP: HA
IB: HA
Input
anti-HA immunoprecipitation

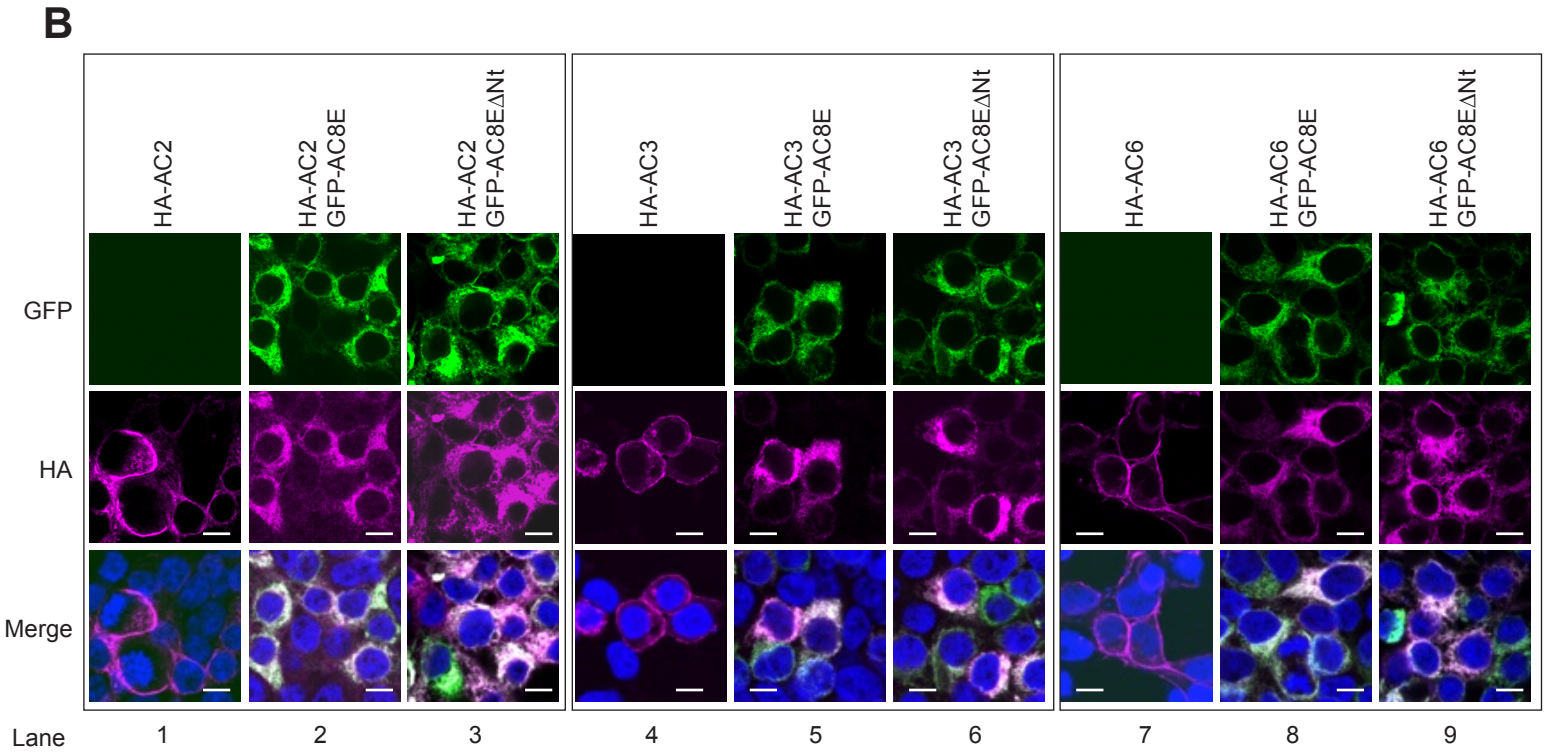
B
HA-AC2
HA-AC2 GFP-AC8E
HA-AC2 GFP-AC8EΔNt
HA-AC3
HA-AC3 GFP-AC8E
HA-AC3 GFP-AC8EΔNt
HA-AC6
HA-AC6 GFP-AC8E
HA-AC6 GFP-AC8EΔNt
GFP
HA
Merge
Lane 1 2 3 4 5 6 7 8 9

Figure 4

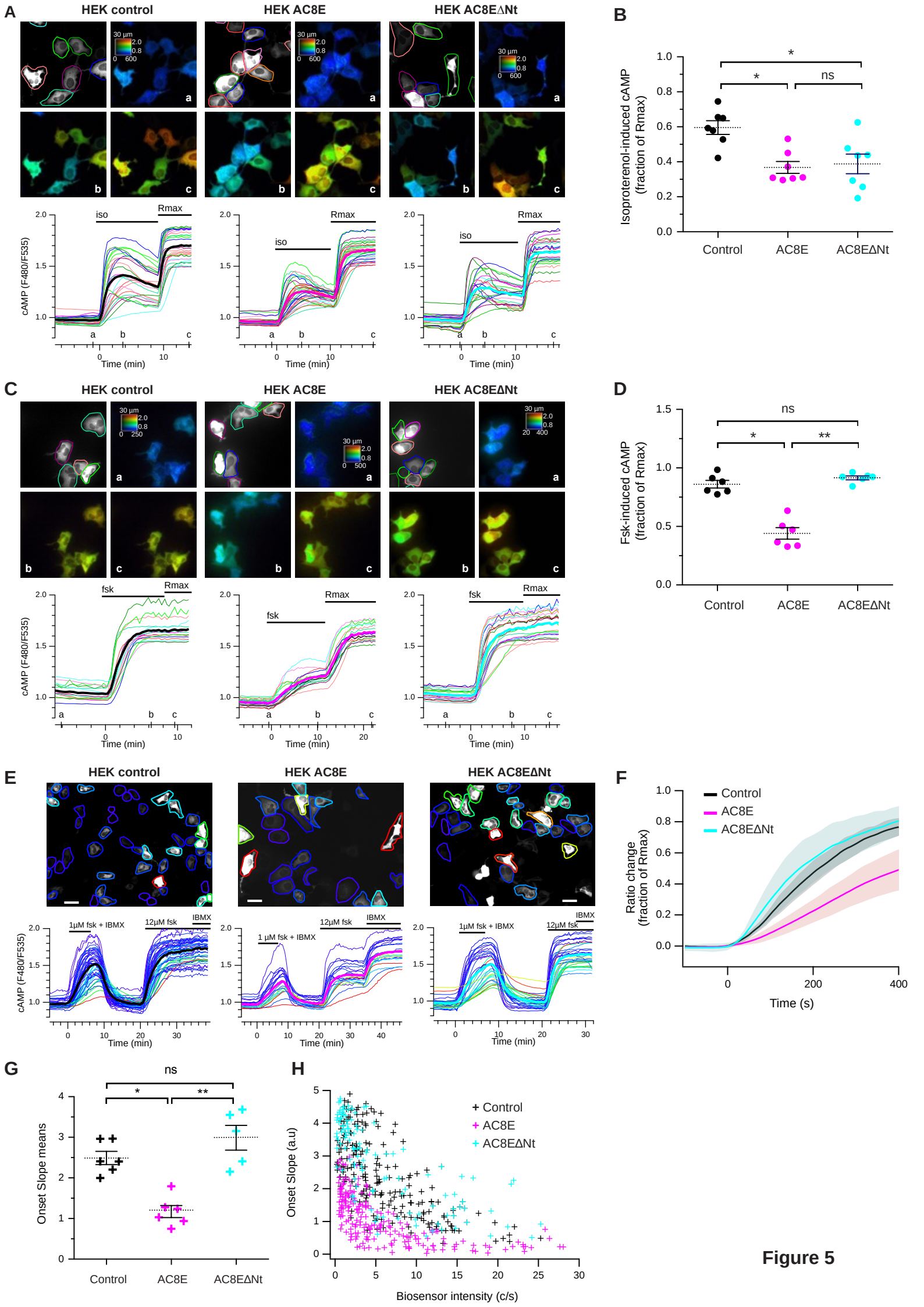
A
HEK control
HEK AC8E
HEK AC8EΔNt
30 µm
2.0
0.8
0
600
a
b
c
iso
Rmax
cAMP (F480/F535)
Time (min)
B
Isoproterenol-induced cAMP
(fraction of Rmax)
*
ns
Control
AC8E
AC8EΔNt
C
HEK control
HEK AC8E
HEK AC8EΔNt
fsk
Rmax
D
Fsk-induced cAMP
(fraction of Rmax)
ns
*
**
E
HEK control
HEK AC8E
HEK AC8EΔNt
1µM fsk + IBMX
12µM fsk
IBMX
F
Control
AC8E
AC8EΔNt
Ratio change
(fraction of Rmax)
Time (s)
G
Onset Slope means
ns
*
**
H
Onset Slope (a.u)
Biosensor intensity (c/s)

Figure 5

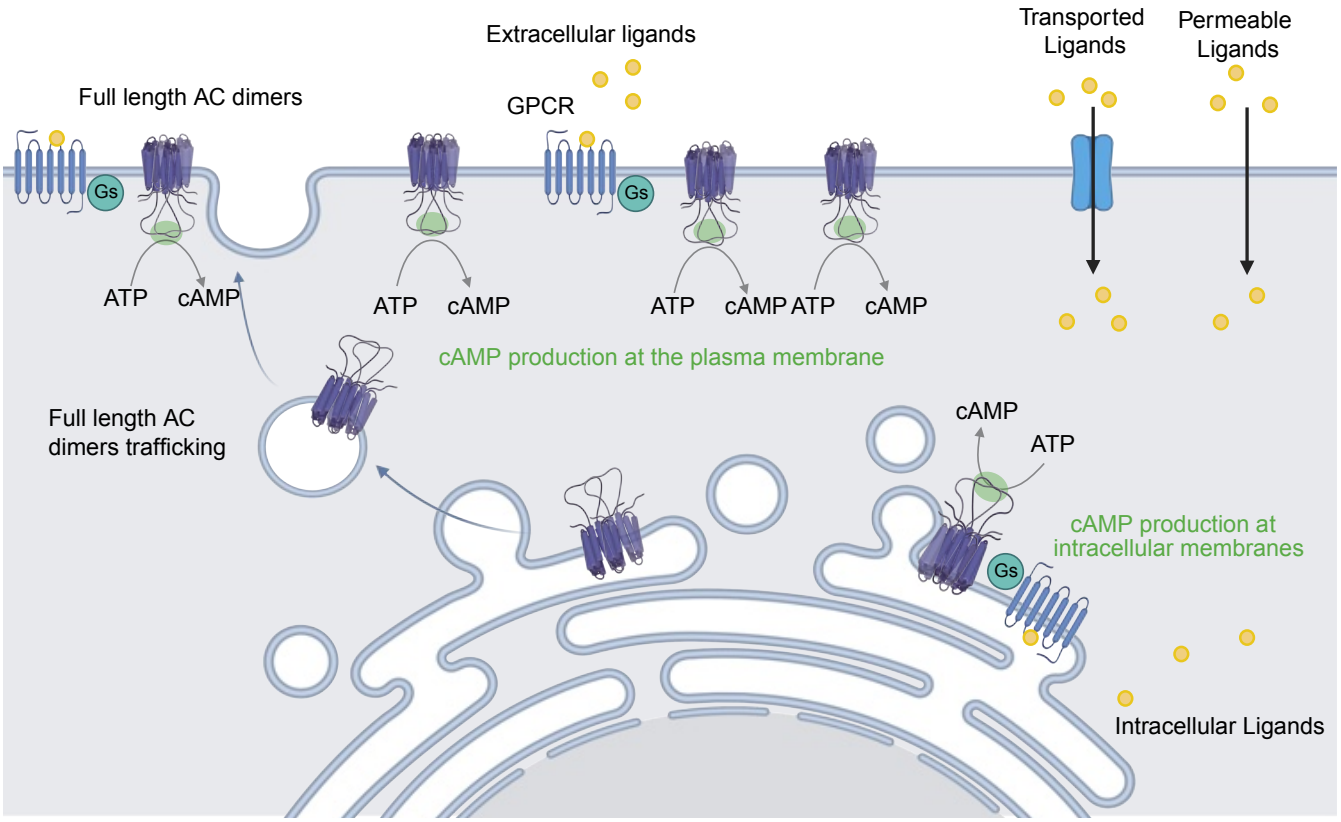

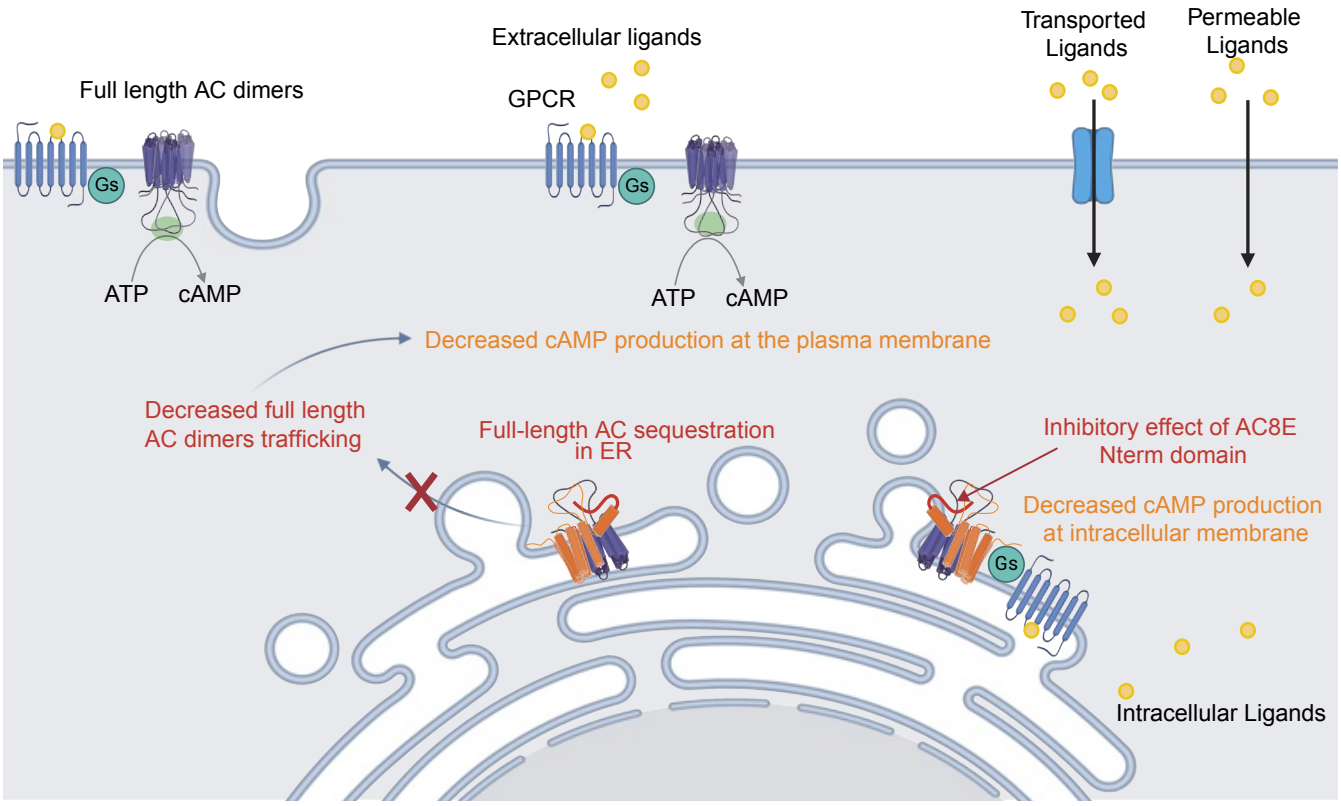

LEGENDS

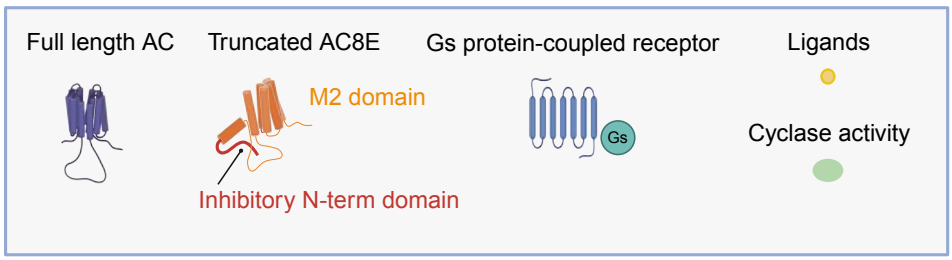

Figure 6

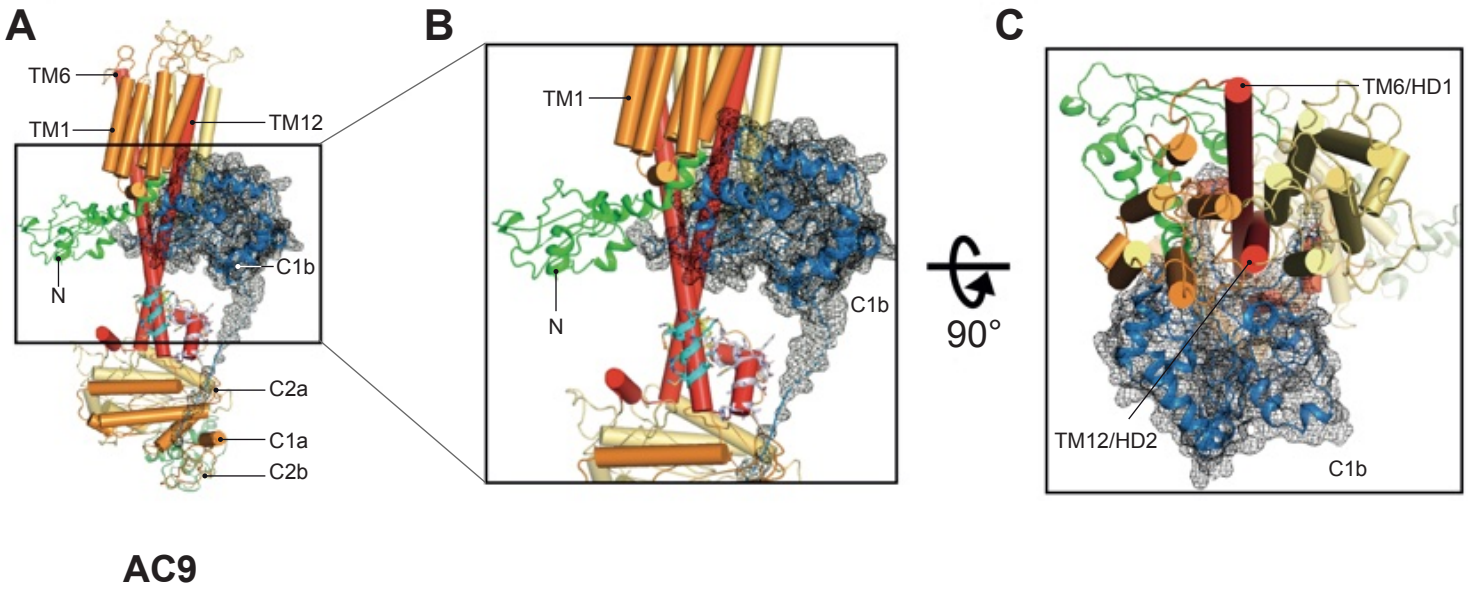

AC9

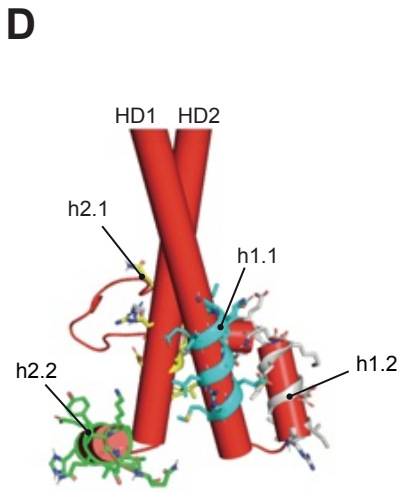

Supplementary Figure S1

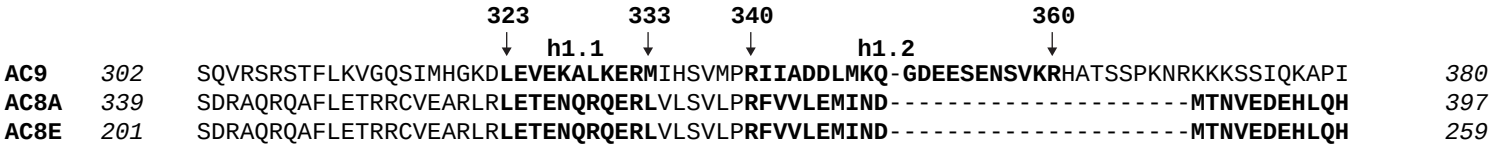

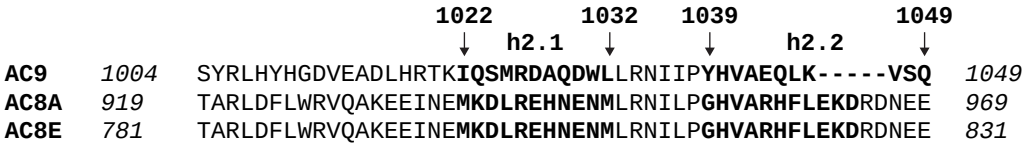

Supplementary Figure S2

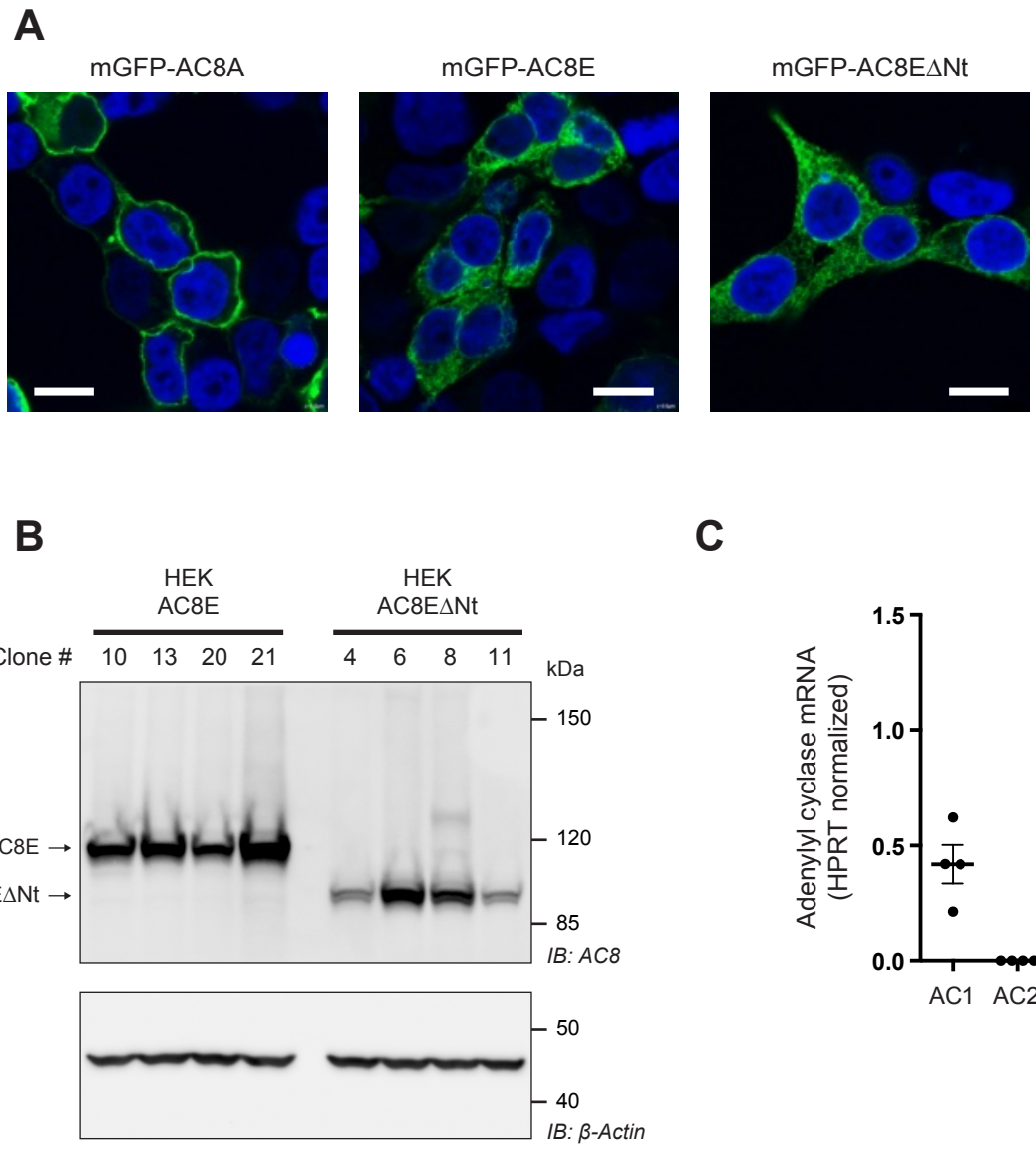

Supplementary Figure S3

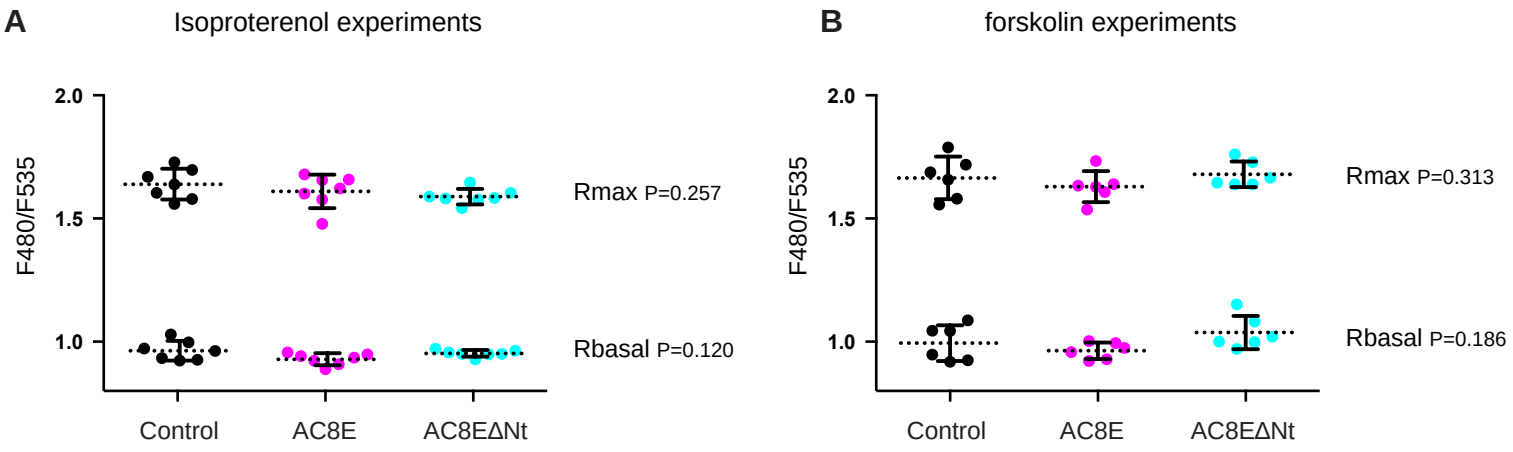

Supplementary Figure S4

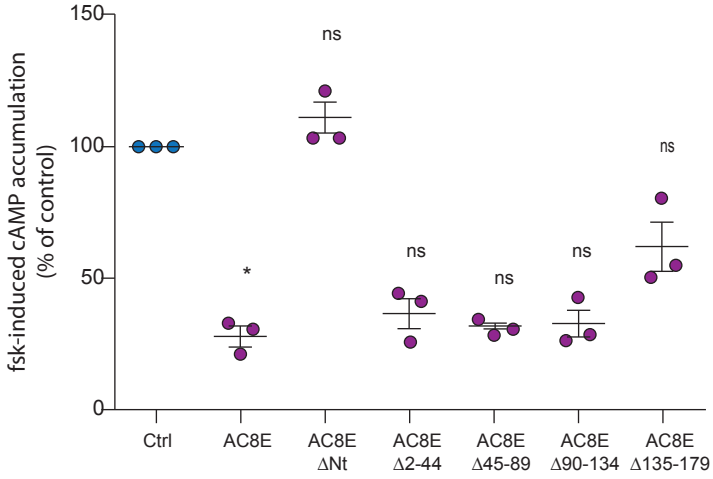

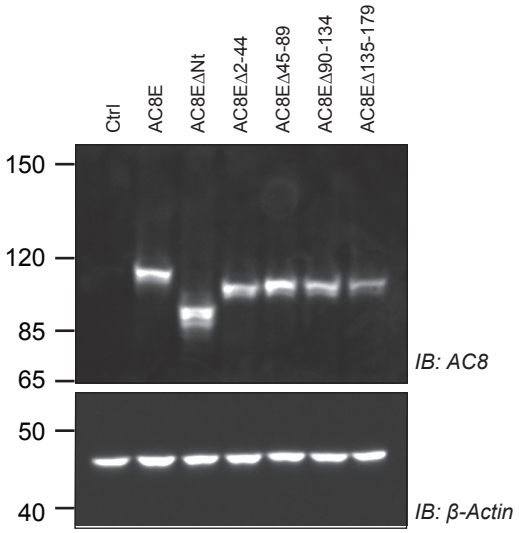

Supplementary Figure S5